


New tool for 21-cm cosmology. II. Investigating the effect of early linear fluctuations

Jordan Flitter^{*} and Ely D. Kovetz

Physics Department, Ben-Gurion University of the Negev, Beer-Sheva 84105, Israel

 (Received 17 September 2023; accepted 13 December 2023; published 9 February 2024)

In the preceding article, we introduce 21cmFirstCLASS, a new code for computing the 21-cm anisotropies, assembled from the merger of the two popular codes 21cmFAST and CLASS. Unlike the standard 21cmFAST, which begins at $z = 35$ with homogeneous temperature and ionization boxes, our code begins its calculations from recombination, evolves the signal through the dark ages, and naturally yields an inhomogeneous box at $z = 35$. In this paper, we validate the output of 21cmFirstCLASS by developing a new theoretical framework which is simple and intuitive on the one hand, but robust and precise on the other hand. As has been recently claimed, using consistent inhomogeneous initial conditions mitigates inaccuracies, which according to our analysis can otherwise reach the $\mathcal{O}(20\%)$ level. On top of that, we also show for the first time that 21cmFAST overpredicts the 21-cm power spectrum at $z \gtrsim 20$ by another $\mathcal{O}(20\%)$, due to the underlying assumption that $\delta_b = \delta_c$, namely that the density fluctuations in baryons and cold dark matter are indistinguishable. We propose an elegant solution to this discrepancy by introducing an appropriate scale-dependent growth factor into the evolution equations. Our analysis shows that this modification will ensure subpercent differences between 21cmFirstCLASS and the Boltzmann solver CAMB at $z \leq 50$ for all scales between the horizon and the Jeans scale. This will enable 21cmFirstCLASS to consistently and reliably simulate the 21-cm anisotropies both in the dark ages and cosmic dawn, for any cosmology.

DOI: [10.1103/PhysRevD.109.043513](https://doi.org/10.1103/PhysRevD.109.043513)

I. INTRODUCTION

It is truly remarkable how much we can learn about our Universe from hyperfine transitions in neutral hydrogen atoms that once permeated the intergalactic medium (IGM). Each said transition results in the emission of a ~ 21 -cm wavelength photon that is redshifted as it propagates to Earth. This is the cosmic 21-cm signal [1–7].

Studies of the 21-cm signal have shown that the rich astrophysical information contained in it can be exploited to learn about the formation of the first galaxies and stars [8–18], probe the epoch of reionization [19–31], and trace the thermal history of the IGM [32–40]. All of that potential lies within the high-frequency bands (~ 50 – 200 MHz) of the 21-cm signal which can be measured by ground-based detectors. Worldwide efforts in pursuit of the signal are ongoing by numerous collaborations. Some of them aim at detecting the 21-cm global signal, like EDGES [41], SARAS [42], REACH [43], LEDA [44], and PRIZM [45], while others, such as LOFAR [46], MWA [47], GMRT [48], PAPER [49], HERA [50], and SKA [51] focus on the spatial structure of the signal. All of these experiments are limited to the cosmological epochs of cosmic dawn and afterward, at redshifts $z \lesssim 35$, since lower frequencies are

obscured by Earth’s ionosphere. In the next decades, radio receivers deployed on the far side of the moon or in lunar orbit [52–60] will give us access to the poorly constrained epoch of the dark ages, enabling us to challenge the very foundations of the standard model of cosmology [Λ cold dark matter (Λ CDM)] [61].

Codes that can compute the 21-cm anisotropies both at the cosmic dawn and the dark ages, like 21cmFirstCLASS, will therefore become invaluable. This code, introduced in the preceding article [62] (hereafter referred to as Paper I), is based on two popular codes widely used in the literature, 21cmFAST [63,64] and CLASS [65]. Unlike the standard 21cmFAST, which begins its calculations at $z = 35$ with homogeneous temperature and ionization boxes, 21cmFirstCLASS is able to begin from recombination and evolve the boxes through the dark ages. Hence, temperature and ionization fluctuations are naturally developed, leading to an inhomogeneous box at $z = 35$. According to Ref. [66] (hereafter referred as JBM23), these early temperature fluctuations can have an important impact on the 21-cm power spectrum at low redshifts.

Currently, the only state-of-the-art code that can calculate these early fluctuations is CAMB, following the work of Ref. [67] (hereafter LC07). Unlike 21cmFirstCLASS, CAMB works in a completely different way; it does not evolve a coeval box, but rather solves the linear coupled

^{*}jordanf@post.bgu.ac.il

Boltzmann-Einstein equations to obtain the fluctuations in Fourier space. This is achievable because in Λ CDM, above $z = 35$, the fluctuations are expected to be linear, i.e., small, and thus higher terms in perturbation theory can be neglected. Assuming that all early fluctuations are indeed linear during the dark ages, consistency requires `21cmFirstCLASS` to agree with `CAMB`.

In this paper, we first quantify the effect of including temperature and ionization fluctuations in `21cmFirstCLASS` as early as recombination, thereby leading to inhomogeneous initial conditions at the onset of cosmic dawn. We then proceed to validate the output of `21cmFirstCLASS` during the dark ages, by comparing its output with `CAMB`. Although a direct comparison between the two codes is the most straightforward approach to do so, it can be affected by different physical effects which are not taken into account in both codes, as well as different approximations that are adopted.

Instead, we take an analytical approach and develop a theoretical framework to predict the output of these two codes. This framework is arguably more tractable than the one presented in LC07 and so allows us to gather new insights on the nature of the linear fluctuations of the 21-cm signal at the relevant scales for 21-cm interferometry.

Our validation process is thus divided into three steps, as schematically presented in Fig. 1. First, we derive the linear fluctuations of all the relevant physical quantities during the dark ages. Second, we compare our scale-independent theory with the output of `21cmFirstCLASS`. And third, we compare our scale-dependent theory with the output of `CAMB`. Because the comparison in the last two steps is successful, we deduce that scale-dependent growth is the only ingredient missing in `21cmFirstCLASS` to make it consistent with `CAMB`. This modification in the code of

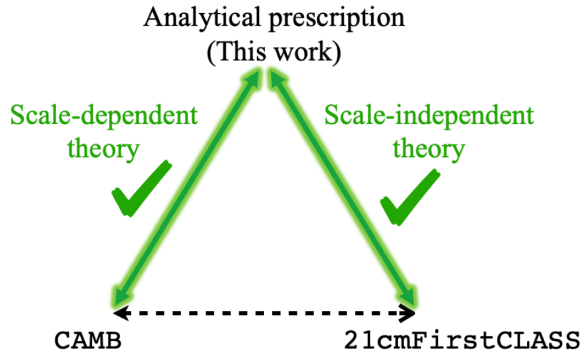


FIG. 1. Schematic representation of our comparison strategy. We compare between the analytical derivations of this work with `21cmFirstCLASS` (`CAMB`), which uses a scale-independent (-dependent) theory for calculating the anisotropies in the 21-cm signal during the dark ages. As these comparisons are successful, our conclusion is that implementing the scale-dependent theory in `21cmFirstCLASS` will make it fully consistent with `CAMB`.

`21cmFirstCLASS` is feasible and will be implemented in its next version, which shall be made public.

The remaining parts of this paper are organized as follows. In Sec. II we quote the standard equations used in 21-cm analysis. In Sec. III we analyze the evolution of early temperature and ionization fluctuations and their impact on the 21-cm power spectrum at low redshifts. In Sec. IV we derive the brightness temperature fluctuations and relate them to the temperature and ionization fluctuations that were discussed at the previous section. In that section we also compare our scale-independent formalism with the output of `21cmFirstCLASS`. In Sec. V we discuss the effect of nonlinearities in the density field on the 21-cm power spectrum. We then compare our scale-dependent formalism with the output of `CAMB` in Sec. VI. We conclude in Sec. VII.

As in Paper I, we adopt in this work the best-fit values for the cosmological parameters from Planck 2018 [68] (without baryon acoustic oscillations), namely we assume a Hubble constant $h = 0.6736$, total matter and baryon-density parameters $\Omega_m = 0.3153$, $\Omega_b = 0.0493$, and a primordial curvature amplitude $A_s = 2.1 \times 10^{-9}$ with a spectral index $n_s = 0.9649$. For the fiducial values of the astrophysical parameters in `21cmFAST`, we adopt the EOS2021 values listed in Table 1 of Ref. [64]. To reduce clutter, we often do not explicitly write the independent arguments of the physical quantities (e.g., redshift, wave number, etc.) and they should be inferred from the context. All of our formulas are expressed in the centimeter-gram-second unit system.

II. 21-CM THEORY

In Paper I we give a brief description of the 21-cm signal physics. Here we are only going to rewrite the fundamental equations that will serve us later in the derivations of this paper. Readers who wish to understand the origin of these equations can find classic reviews in Refs. [1–5].

The 21-cm signal is the measurement of the physical quantity known as the brightness temperature,

$$T_{21} = \frac{T_s - T_\gamma}{1 + z} (1 - e^{-\tau_{21}}), \quad (1)$$

where $T_\gamma \propto (1 + z)$ is the redshift-dependent temperature of the cosmic microwave background (CMB), T_s is the spin temperature, and $\tau_{21} \ll 1$ is the 21-cm optical depth,

$$\tau_{21} = \frac{3\hbar A_{10} c \lambda_{21}^2 (1 - x_e) n_{\text{H}}}{16 H k_B T_s} \left(1 + \frac{1}{H} \frac{d(\hat{\mathbf{n}} \cdot \mathbf{v}_b)}{d(\hat{\mathbf{n}} \cdot \mathbf{x})} \right)^{-1}. \quad (2)$$

Here, c is the speed of light, \hbar is the (reduced) Planck constant, k_B is the Boltzmann constant, H is the redshift-dependent Hubble parameter, $\lambda_{21} \approx 21$ cm is the wavelength of a 21-cm photon, $A_{10} = 2.85 \times 10^{-15} \text{ sec}^{-1}$ is the spontaneous emission coefficient from the excited

hyperfine level to the ground state, and $x_e \equiv n_e/(n_H + n_{\text{He}})$ is the ionization fraction where n_e , n_H , and n_{He} are the free-electron, hydrogen-nuclei, and helium-nuclei number densities, respectively. Finally, the last term accounts for the comoving derivative of the baryons peculiar velocity¹ along the line of sight $\hat{\mathbf{n}}$.

In thermal equilibrium the spin temperature obeys

$$T_s^{-1} = \frac{x_{\text{CMB}} T_\gamma^{-1} + x_{\text{coll}} T_k^{-1} + \tilde{x}_\alpha T_\alpha^{-1}}{x_{\text{CMB}} + x_{\text{coll}} + \tilde{x}_\alpha}, \quad (3)$$

where T_k is the IGM gas kinetic temperature, $T_\alpha \approx T_k$ is the color temperature of Ly α photons, and $x_{\text{CMB}} = (1 - e^{-\tau_{21}})/\tau_{21} \sim 1$, \tilde{x}_α , and x_{coll} are the CMB [69], Ly α [70], and collisional [4] couplings, respectively. The evolution of T_k is determined from

$$\frac{dT_k}{dz} = \frac{dt}{dz} \left[-2HT_k + \Gamma_C(T_\gamma - T_k) + \frac{2}{3} \frac{T_k}{1 + \delta_b} \frac{d\delta_b}{dt} + \epsilon_{\text{ext}} - \frac{T_k}{1 + x_e} \frac{dx_e}{dt} \right], \quad (4)$$

where $dt/dz = -[H(1+z)]^{-1}$, and Γ_C is the Compton heating rate,

$$\Gamma_C \equiv \frac{8\pi^2 \sigma_T (k_B T_\gamma)^4}{45 \hbar^3 c^4 m_e} \frac{x_e}{1 + x_e}, \quad (5)$$

where m_e is the electron mass and σ_T is Thomson cross section. The term ϵ_{ext} in Eq. (4) denotes the heating rates from external sources, mainly x-ray heating (but Ly α and CMB heating rates [69,71,72] can be included), and $\delta_b \equiv \delta\rho_b/\bar{\rho}_b$ is the contrast in the baryon-density fluctuations.

The last equation we need in order to study the fluctuations in the signal during the dark ages is the evolution equation for x_e . In general, this equation is very complicated and tracks the recombination states of both hydrogen and helium, while taking into account excitations to high-order energy levels. These effects have been implemented in the publicly available code HyRec [73,74], which we have incorporated in our 21cmFirstCLASS code (see Paper I for more details). However, we will see in Sec. III that, in order to derive analytically the evolution of temperature and ionization fluctuations, it is sufficient to consider the Peebles effective three-level atom model [75], in which the evolution of x_e is given by

$$\frac{dx_e}{dz} = \frac{dt}{dz} \left[\frac{dx_e}{dt} \Big|_{\text{reio}} + C(\beta_{\text{ion}}(1 - x_e) - \alpha_{\text{rec}} n_H x_e^2) \right], \quad (6)$$

¹Note that in our notation, $\mathbf{v}_b \equiv d\mathbf{x}_b/dt$ is the comoving peculiar velocity of the baryons. The proper comoving velocity is obtained by multiplying that quantity with the scale factor.

where α_{rec} is the recombination rate (in units of cm³/sec), β_{ion} is the early photoionization rate, and C is the Peebles coefficient (see Appendix A for more details on the Peebles coefficient). The term $dx_e/dt|_{\text{reio}}$ represents the reionization rate at late times. At early times (prior the epoch of reionization), the recombination rate and photoionization rates were in equilibrium, and thus

$$\beta_{\text{ion}} = \alpha_{\text{rec}} \left(\frac{m_e k_B T_\gamma}{2\pi \hbar^2} \right)^{3/2} e^{-\epsilon_0/(k_B T_\gamma)}, \quad (7)$$

where $\epsilon_0 = 13.6$ eV denotes the ionization energy of the hydrogen atom from its ground state.

III. EARLY TEMPERATURE AND IONIZATION FLUCTUATIONS

One of the advantages of 21cmFirstCLASS is that it allows one to study nonlinear evolution above $z = 35$ in models beyond Λ CDM. It is tempting, however, to examine if small, linear Λ CDM fluctuations prior to $z = 35$ can induce a measurable impact on the brightness temperature during the cosmic dawn or afterward.

To study the evolution of early linear temperature fluctuations, let us consider the temperature evolution equation (4) prior to cosmic dawn, when $\epsilon_{\text{ext}} = 0$. We also neglect the last term in Eq. (4), and we will show that it has indeed a negligible effect on the analysis contained in this section. Thus

$$\frac{dT_k}{dz} = \frac{2T_k}{1+z} - \frac{\Gamma_C(T_\gamma - T_k)}{H(1+z)} + \frac{2}{3} \frac{T_k}{1 + \delta_b} \frac{d\delta_b}{dz}. \quad (8)$$

We now expand $T_k = \bar{T}_k + \delta T_k$, $\Gamma_C = \bar{\Gamma}_C + \delta\Gamma_C$ in linear perturbation theory. Throughout this work we shall assume that the CMB temperature is homogeneous, that is we assume $\delta T_\gamma \equiv 0$. This is an excellent approximation because at the relevant subhorizon scales and redshifts the linear fluctuations in the CMB temperature are more negligible than all other fluctuations. The evolution equation for the background temperature \bar{T}_k is similar to Eq. (8), though without the last term, while the evolution equation for δT_k is

$$\frac{d\delta T_k}{dz} = \frac{2\delta T_k}{1+z} + \frac{\bar{\Gamma}_C \delta T_k}{H(1+z)} - \frac{\delta\Gamma_C(T_\gamma - \bar{T}_k)}{H(1+z)} + \frac{2}{3} \bar{T}_k \frac{d\delta_b}{dz}. \quad (9)$$

We see that the Compton heating term in Eq. (8) induces the second and third terms on the rhs of Eq. (9), which we refer to collectively as ‘‘Compton fluctuations.’’ From Eq. (5) it is straightforward to find that the linear fluctuations in the Compton heating rate are given by

$$\delta\Gamma_C = \bar{\Gamma}_C \frac{\delta x_e}{\bar{x}_e(1 + \bar{x}_e)}, \quad (10)$$

where $x_e = \bar{x}_e + \delta x_e$. Thus, Eq. (9) becomes [76]

$$\begin{aligned} \frac{d\delta T_k}{dz} &= \frac{2\delta T_k}{1+z} + \frac{\bar{\Gamma}_C \delta T_k}{H(1+z)} - \frac{\bar{\Gamma}_C(T_\gamma - \bar{T}_k)}{H(1+z)} \frac{\delta x_e}{\bar{x}_e(1+\bar{x}_e)} \\ &+ \frac{2}{3} \bar{T}_k \frac{d\delta_b}{dz}. \end{aligned} \quad (11)$$

For cold dark matter, the linear density fluctuations evolve in an almost scale-invariant fashion (especially at high redshifts before the baryons had settled in the CDM gravitational potential wells) according to $\delta_c(z) = D(z)\delta_0$, where $D(z)$ is the scale-independent growth factor and $\delta_0 \equiv \delta_c(z=0)$. For the baryons, we now define a scale-dependent growth factor $\mathcal{D}_b(k, z)$ as

$$\mathcal{D}_b(k, z) \equiv \mathcal{T}_{b/c}(k, z)D(z), \quad (12)$$

where $\mathcal{T}_{b/c}(k, z) \equiv \mathcal{T}_b(k, z)/\mathcal{T}_c(k, z)$ is the ratio between the baryon-density and the CDM-density transfer functions, so that $\delta_b(k, z) = \mathcal{T}_{b/c}(k, z)\delta_c(z) = \mathcal{D}_b(k, z)\delta_0$.

In Fig. 2 we show $\mathcal{T}_{b/c}(k, z)$ as a function of redshift at the relevant scales for 21-cm interferometers. Initially, at high redshifts ($z \sim 1000$), $\delta_b \ll \delta_c$, or $\mathcal{T}_{b/c}(k, z) \ll 1$, since the baryons have recently been freed from the strong coupling with the CMB; before the baryons decoupled from the CMB photons, their density contrast was oscillating in a scale-dependent manner, while the CDM-density contrast was continuously growing, especially after matter-radiation equality ($z \approx 3300$) where $D(z) \propto (1+z)^{-1}$. Afterward, for scales larger than the Jeans scale, the baryons can be considered as collisionless particles and they obey the same equation of motion as CDM. Therefore, for the scales of interest, the baryons and the CDM become indistinguishable at low redshifts, after enough time has passed and their different initial conditions no longer play an important role in their evolution. Hence, at low redshifts $\delta_b \rightarrow \delta_c$ and $\mathcal{T}_{b/c}(k, z) \rightarrow 1$. This is the assumption made in the standard 21cmFAST, where the simulation begins at $z = 35$. However, the error induced by this assumption can

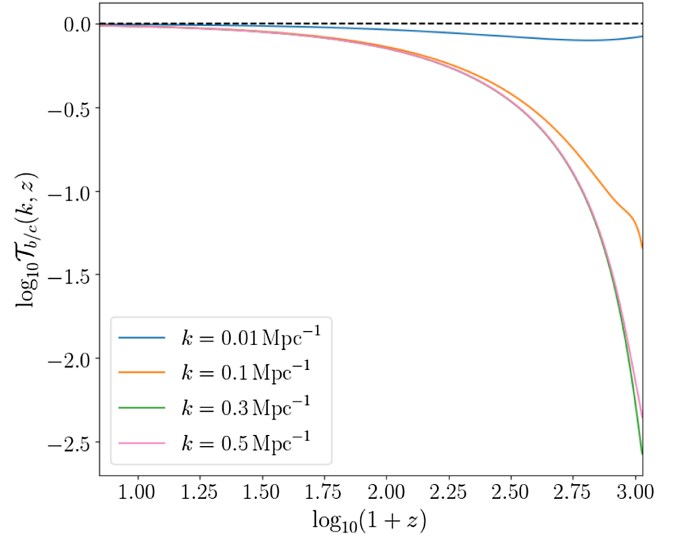


FIG. 2. The ratio between the baryon transfer function $\mathcal{T}_b(k, z)$ and the CDM transfer function $\mathcal{T}_c(k, z)$ as a function of redshift, for three different scales. For the smallest scales shown here (not including $k = 0.01 \text{ Mpc}^{-1}$), $\mathcal{T}_{b/c}(k, z) = 0.97, 0.96, 0.92, 0.88$ for $z = 6, 10, 20, 35$, respectively. At smaller scales, the resulting curve almost overlaps with the red curve of $k = 0.5 \text{ Mpc}^{-1}$. This figure was made with CLASS.

be of the order of $\mathcal{O}(10\%)$ for $z \gtrsim 20$. Since the 21-cm power spectrum $\Delta_{21}^2(k, z)$ is proportional to $\mathcal{T}_b^2(k, z)$, at least at redshifts prior to the nonlinear cosmic dawn epoch [cf. Eq. (40)], this error becomes $\mathcal{O}(20\%)$ in the evaluation of $\Delta_{21}^2(k, z)$. Another interesting feature that can be seen in Fig. 2 is that the relative suppression of $\mathcal{T}_b(k, z)$ at high redshifts is not necessarily stronger at smaller scales (or larger k). This is because different modes begin with different initial conditions, depending on their oscillatory phase at the moment of decoupling. However, adiabatic fluctuations imply $\delta_b \equiv \delta_c$ and $\mathcal{T}_{b/c}(k, z) \equiv 1$ on super-horizon scales [77].

The solution for δT_k in Eq. (11) can be expressed analytically in the following way:

$$\begin{aligned} c_T(k, z) &= -\frac{2}{3} \frac{(1+z)^2}{\bar{T}_k(z)\mathcal{D}_b(k, z)} \int_z^\infty dz' \frac{\bar{T}_k(z')}{(1+z')^2} \frac{d\mathcal{D}_b(k, z')}{dz'}, \\ &- \frac{(1+z)^2}{\bar{T}_k(z)\mathcal{D}_b(k, z)} \int_z^\infty dz' \frac{\bar{\Gamma}_C(z')\bar{T}_k(z')\mathcal{D}_b(k, z')}{(1+z')^3 H(z')} c_T(k, z'), \\ &+ \frac{(1+z)^2}{\bar{T}_k(z)\mathcal{D}_b(k, z)} \int_z^\infty dz' \frac{\bar{\Gamma}_C(z')[T_\gamma(z') - \bar{T}_k(z')]\mathcal{D}_b(k, z')}{(1+z')^3 H(z')[1+\bar{x}_e(z')]} c_{x_e}(k, z'), \end{aligned} \quad (13)$$

where $c_T \equiv \delta T_k/(\bar{T}_k \cdot \delta_b)$ and $c_{x_e} \equiv \delta x_e/(\bar{x}_e \cdot \delta_b)$. Note that Eq. (13) can be compared to Eq. (47) in JBM23 where Compton fluctuations were neglected and the second and third terms are absent. Moreover, we see that c_T is a

scale-dependent quantity due to the nontrivial scale dependence of $\mathcal{D}_b(k, z)$. The first term in Eq. (13) represents adiabatic temperature fluctuations due to structure growth. This term is positive because $d\mathcal{D}_b/dz < 0$.

The sign of the second and third terms is not clear at first sight and depends on the sign of c_T and c_{x_e} . We claim, however (and we verify this statement below), that these two terms give a *negative* contribution to c_T and thus lower its value. The second term is negative because $c_T > 0$, as overdense regions are expected to be overheated. The third term is negative because $c_{x_e} < 0$, as the recombination rate in overdense regions is higher and therefore the number of free electrons is reduced.

The fact that c_T depends on the integrated histories of both c_T and c_{x_e} complicates its evaluation compared to the case where there are no Compton fluctuations. We will see below, however, that including all sources of fluctuations is absolutely necessary in order to obtain the correct solution.

In order to continue with the analytic derivation, we must include the differential equation for δx_e . We shall not attempt to find the exact evolution equation for x_e , and instead we shall adopt the simpler Peebles model, Eq. (6). Omitting the late time reionization term, the evolution equation for x_e reads

$$\begin{aligned} \frac{dx_e}{dz} &= \frac{\mathcal{C}}{H(1+z)} (\alpha_{\text{rec}} n_{\text{H}} x_e^2 - \beta_{\text{ion}} (1 - x_e)) \\ &= \left. \frac{dx_e}{dz} \right|_{\text{rec}} + \left. \frac{dx_e}{dz} \right|_{\text{ion}}, \end{aligned} \quad (14)$$

where we identified the recombination and ionization contributions to dx_e/dz . We then find, after working out the algebra, that [76]

$$\begin{aligned} \frac{d\delta x_e}{dz} &= \left(\left. \frac{2 d\bar{x}_e}{\bar{x}_e dz} \right|_{\text{rec}} - \left. \frac{1 d\bar{x}_e}{1 - \bar{x}_e dz} \right|_{\text{ion}} \right) \delta x_e \\ &\quad + \left. \frac{d\bar{x}_e}{dz} \right|_{\text{rec}} \delta_b + \left(\frac{\delta \mathcal{C}}{\bar{\mathcal{C}}} + \frac{\delta \alpha_{\text{rec}}}{\bar{\alpha}_{\text{rec}}} \right) \frac{d\bar{x}_e}{dz}. \end{aligned} \quad (15)$$

In the name of brevity, we now ignore fluctuations in the Peebles coefficient \mathcal{C} , although they have non-negligible contributions to δx_e at high redshifts. We provide more details on the calculation of $\delta \mathcal{C}$ in Appendix A. In addition, we assume α_{rec} is the case-B recombination rate and a function of T_k only, $\alpha_{\text{rec}} = \alpha_B(T_k)$. With these assumptions, we can write Eqs. (11) and (15) in matrix form,

$$\begin{aligned} \frac{d\delta v(k, z)}{dz} &= A(z) \delta v(k, z) + B(k, z) \\ &= \begin{bmatrix} A_{11}(z) & A_{12}(z) \\ A_{21}(z) & A_{22}(z) \end{bmatrix} \delta v(k, z) + \begin{bmatrix} B_1(k, z) \\ B_2(k, z) \end{bmatrix}, \end{aligned} \quad (16)$$

where $\delta v^T = [\delta v_1 \delta v_2] \equiv [\delta T_k \delta x_e]$ and the elements of the matrices A and B are

$$A_{11}(z) = \frac{2}{1+z} + \frac{\bar{\Gamma}_C}{H(1+z)}, \quad (17)$$

$$A_{12}(z) = -\frac{\bar{\Gamma}_C(T_\gamma - \bar{T}_k)}{H(1+z)} \frac{1}{\bar{x}_e(1 + \bar{x}_e)}, \quad (18)$$

$$A_{21}(z) = \frac{\partial \ln \alpha_B(\bar{T}_k)}{\partial \bar{T}_k} \frac{d\bar{x}_e}{dz}, \quad (19)$$

$$A_{22}(z) = \left. \frac{2 d\bar{x}_e}{\bar{x}_e dz} \right|_{\text{rec}} - \left. \frac{1 d\bar{x}_e}{1 - \bar{x}_e dz} \right|_{\text{ion}}, \quad (20)$$

$$B_1(k, z) = \frac{2}{3} \bar{T}_k \frac{d\mathcal{D}_b(k, z)}{dz} \delta_0, \quad (21)$$

$$B_2(k, z) = \mathcal{D}_b(k, z) \left. \frac{d\bar{x}_e}{dz} \right|_{\text{rec}} \delta_0. \quad (22)$$

Then, Eq. (16) has a closed form solution, which for zero initial conditions $\delta v(k, z \rightarrow \infty) = 0$ reads

$$\delta v(k, z) = - \int_z^\infty dz' \exp \left[- \int_z^{z'} A(z'') dz'' \right] B(k, z'). \quad (23)$$

Note that, in the absence of Compton fluctuations, Eq. (23) is consistent with the first line of Eq. (13) [and Eq. (47) in JBM23]. Because $B(k, z) \propto \delta_0$, $\delta v(k, z) \propto \delta_0$, and for the calculation of c_T we can choose any arbitrary nonzero value of δ_0 when we evaluate Eq. (23), we then get

$$c_T(k, z) = \frac{\delta v_1(k, z)}{\bar{T}_k(z) \mathcal{D}_b(k, z) \delta_0}, \quad (24)$$

$$c_{x_e}(k, z) = \frac{\delta v_2(k, z)}{\bar{x}_e(z) \mathcal{D}_b(k, z) \delta_0}. \quad (25)$$

Note that c_{x_e} is an inevitable by-product of the calculation of c_T .

In what follows, we solve numerically² Eq. (16) from recombination, defined by $\bar{x}_e(z_{\text{rec}}) \equiv 0.1$, while assuming zero initial conditions [76]. In addition, in our analytical calculations we adopt the recombination model of RECFAST [78–80],

$$\alpha_B(T_k) = F_\alpha \frac{a_\alpha (T_k/10^4 \text{K})^{b_\alpha} \text{cm}^3}{1 + c_\alpha (T_k/10^4 \text{K})^{d_\alpha} \text{sec}}, \quad (26)$$

where $a_\alpha = 4.309 \times 10^{-13}$, $b_\alpha = -0.6166$, $c_\alpha = 0.6703$, $d_\alpha = 0.5300$, and $F_\alpha = 1.125$ is a fudge factor to reproduce the result of a multilevel atom calculation [74,81].

²While Eq. (23) is analytically correct, we found it numerically challenging to evaluate the double integration to good precision.

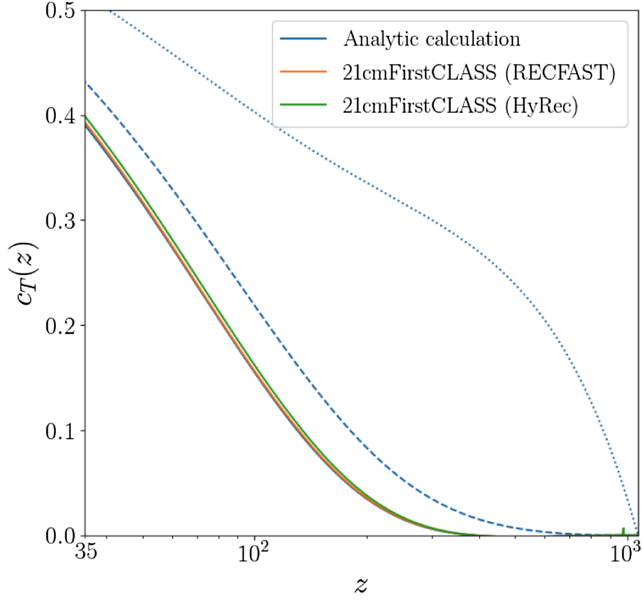


FIG. 3. The scale-independent $c_T(z)$. The solid blue curve is the solution to Eq. (16) [or Eq. (23)] when accounting for Peebles fluctuations (see Appendix A), while the orange (green) curve corresponds to the median of the $c_T(\mathbf{x}, z)$ box in 21cmFirstCLASS when the considered recombination model is from RECFAST (HyRec). For comparison, we also show the contribution of Compton fluctuations to the solution. The blue dotted curve corresponds to accounting only for the first row in Eq. (13), the dashed blue curve corresponds to accounting for the first two rows in Eq. (13), and the solid blue curve corresponds to accounting for all three rows in Eq. (13).

A. Scale independence

In order to gain some intuition for the qualitative features in the solution for c_T and c_{x_e} , let us begin the discussion by assuming that these quantities evolve in a scale-independent manner, i.e., $c_T(k, z) = c_T(z)$, $c_{x_e}(k, z) = c_{x_e}(z)$. Mathematically speaking, this is equivalent to setting $\mathcal{T}_{b/c}(k, z) \equiv 1$, valid only on superhorizon scales. However, it is important to bear in mind that on these scales the fluctuations in the CMB temperature cannot be ignored, as we do in our analysis.

For the scale-independent evolution scenario, the solutions for $c_T(z)$ and $c_{x_e}(z)$ are presented by the solid blue curves in Figs. 3 and 4. As expected, $c_T(z) > 0$ and $c_{x_e}(z) < 0$. Therefore, as can be seen from Eq. (13), Compton fluctuations tend to decrease the value of $c_T(z)$ considerably compared to the case when these fluctuations are not taken into account (represented by the blue dashed and dotted curves in Fig. 3). In addition, we see that Compton fluctuations are responsible for driving $c_T(z)$ to zero at high redshifts. This is physically well understood; at high redshifts, $z \gtrsim 400$, T_k is strongly coupled to the homogeneous T_γ (see Fig. 1 in Paper I), hence $c_T(z) \approx 0$ at these redshifts. And indeed, at $z \sim 400$, once T_k begins to depart from T_γ , $c_T(z)$ begins to grow via the source term of

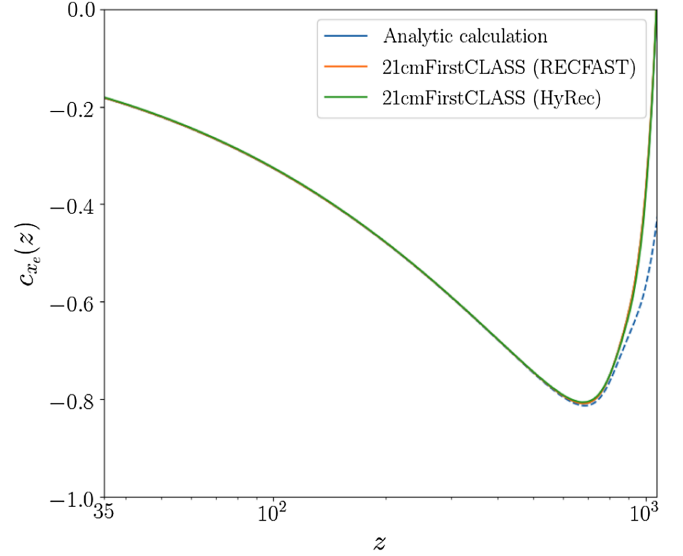


FIG. 4. The scale-independent $c_{x_e}(z)$. The blue curve is the solution to Eq. (16) [or Eq. (23)] when accounting for Peebles fluctuations (see Appendix A), while the orange (green) curve corresponds to the median of the $c_{x_e}(\mathbf{x}, z)$ box in 21cmFirstCLASS when the considered recombination model is from RECFAST (HyRec). The calculation of all solid curves begins at $z_{\text{rec}} = 1069$ [corresponds to $\bar{x}_e(z_{\text{rec}}) = 0.1$], while the calculation of the blue dashed curve begins at $z = 1200$.

Eq. (21). Eventually, it reaches ~ 0.39 at $z = 35$. In fact, we find that, at the vicinity of $z = 35$, $c_T(z)$ can be approximated by the following fit:

$$c_T(z) \approx 0.39 - 0.0056(z - 35) \quad (\text{this work}). \quad (27)$$

This fit is more precise than the fit found in JBM23 (originally derived in Ref. [82]),

$$c_T(z) \approx 0.43 - 0.006(z - 35) \quad (\text{JBM23}). \quad (28)$$

The fit of JBM23, which is now used by default in the public version of 21cmFAST (version 3.3.1) to account for early temperature fluctuations, is consistent with our calculations when the fluctuations in x_e are ignored (the dashed curve in Fig. 3 indeed reaches 0.43 at $z = 35$).

Unlike the monotonous growth of $c_T(z)$, the $c_{x_e}(z)$ curve exhibits a minimum at $z \sim 700$. The origin for this minimum is due to the following. We find that $\delta_{x_e} \equiv \delta x_e / \bar{x}_e$ is monotonously decreasing toward lower negative values, but its rate of decrease is substantially higher above $z \sim 700$. Since during matter domination the decrease in $D^{-1}(z)$ is roughly constant, $D^{-1}(z) \propto (1+z)$, which is faster (slower) than the decreasing rate of δ_{x_e} at $z \lesssim 700$ ($z \gtrsim 700$), the slope of $c_{x_e}(z) \propto \delta_{x_e}(z)D^{-1}(z)$ changes its sign at $z \sim 700$. This does not happen in the $c_T(z)$ curve; between $35 \leq z \leq 400$ the growth in $\delta_{T_k} \equiv \delta T_k / \bar{T}_k$ is always faster than the growth in $D(z)$.

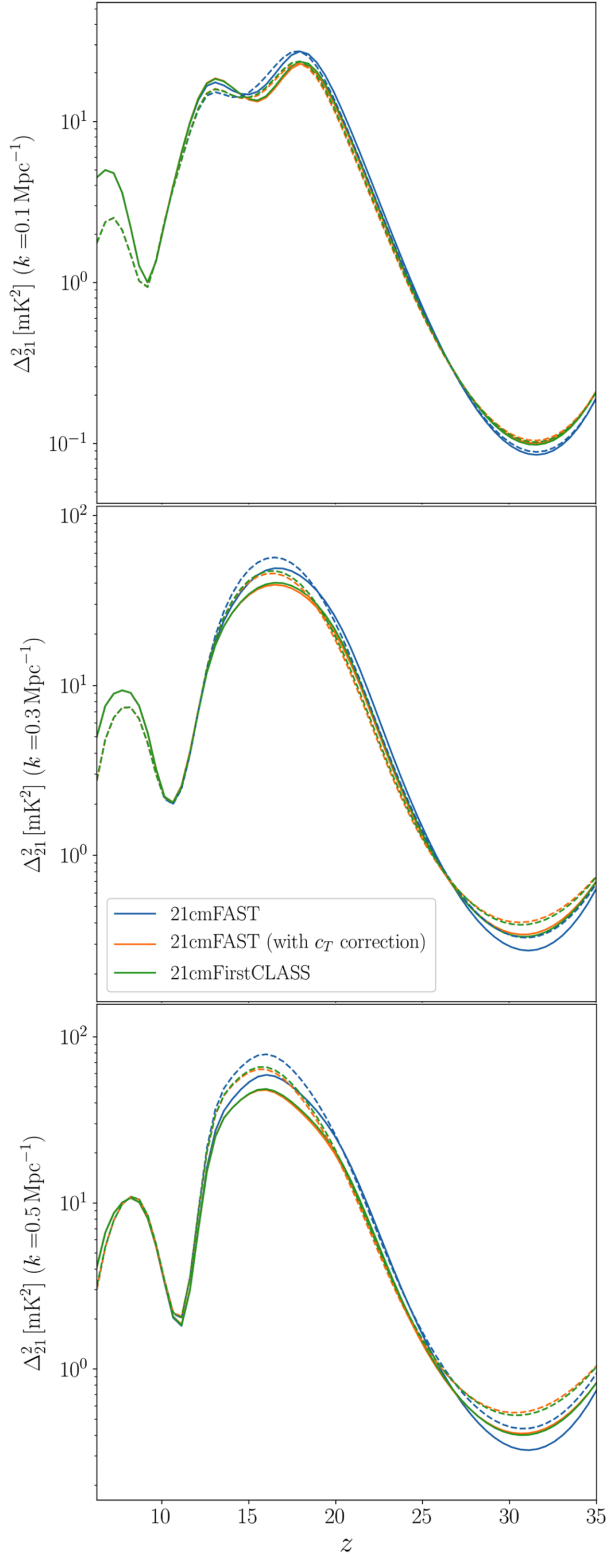


FIG. 5. Comparison of the 21-cm power spectrum between 21cmFirstCLASS and 21cmFAST, for three different wave numbers. The blue (orange) curves show the output of 21cmFAST without (with) the c_T correction, given by the fit of JBM23 [Eq. (28)]. The green curve is the output of 21cmFirstCLASS. Solid (dashed) curves correspond to evolving the density field with 2LPT (linearly). See more details on 2LPT in Sec. V.

Figure 4 displays an unphysical behavior; even though $c_{x_e}(z)$ begins at zero, its derivative does not. Of course, there is no reason to believe that $c_{x_e}(z)$ vanishes exactly at our initial redshift ($z = 1069$), and it is an indication that the calculation has to begin at a higher redshift [76]. We show, however, in Fig. 4 that if we begin the evolution at $z = 1200$, the result remains the same after the turning point at $z \sim 700$. Nevertheless, as we shall see in Sec. IV, c_{x_e} will only have a small effect on the brightness temperature fluctuations at low redshifts, and we will therefore not concern ourselves with obtaining the correct solution for c_{x_e} at redshifts higher than $z \sim 700$.

We also make a comparison in Figs. 3 and 4 between our analytical solution and the output from 21cmFirstCLASS. To achieve the latter, we compute the redshift-dependent median of the coeval boxes $c_T(\mathbf{x}, z)$ and $c_{x_e}(\mathbf{x}, z)$ at each redshift iteration. When we disable HyRec in 21cmFirstCLASS and adopt our simple toy model for the evolution of x_e , the agreement between 21cmFirstCLASS and the scale-independent theory is excellent, especially when inspecting the $c_{x_e}(z)$ curve. For $c_T(z)$, minor differences can be seen at low redshifts. There could be two reasons for this tiny discrepancy; either small nonlinear fluctuations slightly shift the median of the $c_T(\mathbf{x}, z)$ box, or it could be the consequence of small numerical errors that increase as the box evolves.

Regardless, these differences are smaller than the errors due to the approximated recombination model. Activating HyRec in 21cmFirstCLASS results in increasing slightly the value of $c_T(z)$, most likely due to a more precise evolution of \bar{T}_k at high redshifts. Note, however, that because the absolute errors in $c_T(z)$ remain roughly constant over a wide redshift range, the relative errors are significantly larger at higher redshifts. Specifically, at $z = 35$ ($z = 100$) the error in $c_T(z)$ is $\sim 1\%$ ($\sim 4\%$). This small discrepancy will become relevant in our discussion in Sec. VI, where we make a comparison with CAMB.

B. The 21-cm power spectrum in 21cmFirstCLASS

Now that we have established the consistency of 21cmFirstCLASS, at least when linear, scale-free, early temperature, and ionization fluctuations are considered, a natural question arises: do these early fluctuations alter the observable, the 21-cm power spectrum at low redshifts, at a significant level? In other words, does the state of the box at $z = 35$ matter for its evolution afterward? To answer these questions, we calculate with 21cmFirstCLASS the 21-cm power spectrum, given by

$$\Delta_{21}^2(k, z) = \frac{k^3 \bar{T}_{21}^2(z) P_{21}(k, z)}{2\pi^2}, \quad (29)$$

where \bar{T}_{21} is the global brightness temperature and $P_{21}(k, z)$ is the angle-averaged Fourier transform of the

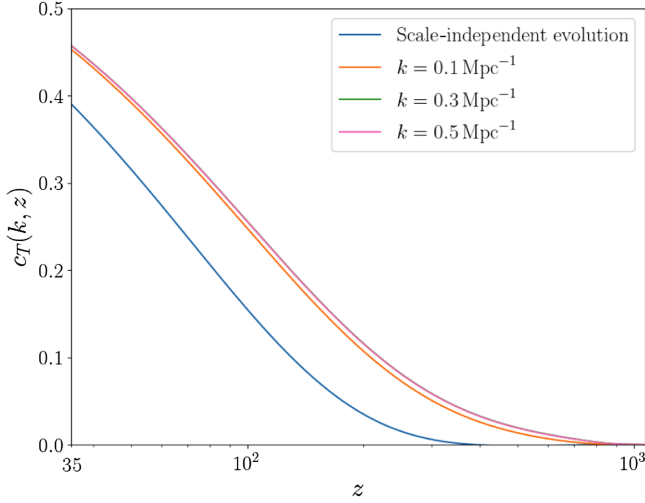


FIG. 6. The scale-dependent $c_T(k, z)$. For comparison, we show the scale-independent $c_T(z)$ with a blue curve (identical to the blue curve in Fig. 3). The green curve of $k = 0.3 \text{ Mpc}^{-1}$ completely overlaps with the pink curve of $k = 0.5 \text{ Mpc}^{-1}$.

two-point correlation function $\langle \delta_{21}(\mathbf{x}, z) \delta_{21}(\mathbf{x}', z) \rangle$, while δ_{21} is the local contrast in the brightness temperature, $\delta_{21}(\mathbf{x}, z) \equiv T_{21}(\mathbf{x}, z) / \bar{T}_{21}(z) - 1$. We use the POWERBOX package [83] to compute $\Delta_{21}^2(k, z)$ from chunks of the light cone box of 21cmFirstCLASS.

Our conclusions are shown in Fig. 5. The blue curves represent the output of the standard 21cmFAST, where homogeneous T_k and x_e boxes are assumed at $z = 35$. In comparison, we also plot the 21-cm power spectrum of 21cmFirstCLASS (which begins with homogeneous boxes at $z_{\text{rec}} = 1069$). At $25 \lesssim z \lesssim 35$, the early fluctuations lead to an enhancement of $\mathcal{O}(10\%)$. In Sec. IV we will understand the origin of this enhancement. However, as we enter the nonlinear regime, the opposite trend can be seen at $12 \lesssim z \lesssim 25$, where early fluctuations cause a suppression of $\mathcal{O}(20\%)$ in the power spectrum. Afterward, at $z \lesssim 12$, the highly nonlinear fluctuations of the star formation rate density (SFRD) become dominant and the initial conditions of the box at $z = 35$ are forgotten.

We also show in Fig. 5 the 21-cm power spectrum of the updated version of 21cmFAST, where the fit of JBM23 [Eq. (28)] has been implemented in the code to generate an inhomogeneous T_k box at $z = 35$. We see that the fit of JBM23 captures very well the power spectrum of 21cmFirstCLASS, even though this fit is slightly different than ours, Eq. (27). Moreover, it is interesting that the 21-cm power spectrum is insensitive to early fluctuations in x_e . We will understand the reason for this in Sec. IV.

C. Scale dependence

Although Figs. 3 and 4 show a nice agreement between 21cmFirstCLASS and the scale-independent theory, the

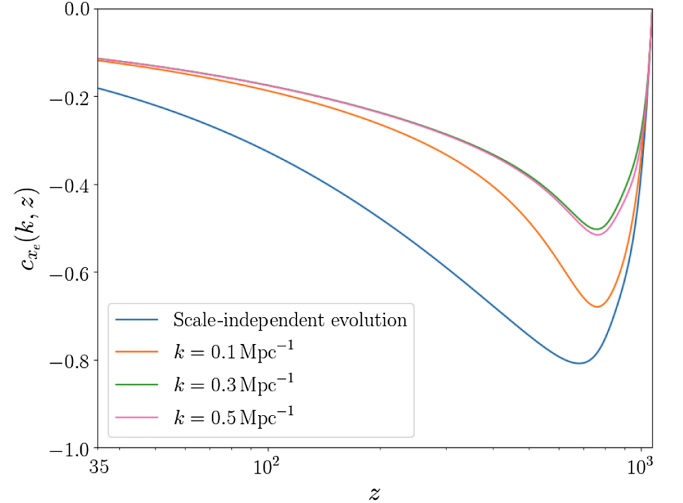


FIG. 7. The scale-dependent $c_{x_e}(k, z)$. For comparison, we show the scale-independent $c_{x_e}(z)$ with a blue curve (identical to the blue curve in Fig. 4).

assumption of $\mathcal{T}_{b/c}(k, z) \equiv 1$ has to be relaxed if we wish to find the correct c_T and c_{x_e} . We do that now. Using our analytical formalism above, we solve for $c_T(k, z)$ and $c_{x_e}(k, z)$, focusing on scales relevant for 21-cm interferometers. The results are shown in Figs. 6 and 7.

Let us analyze first how c_{x_e} depends on scale. From Eq. (22), we can see that the source term of δx_e is suppressed when $\mathcal{D}_b(k, z)$ is considered instead of the scale-independent growth factor $D(z)$. Thus, we can expect that, on scales for which $\mathcal{T}_{b/c}(k, z)$ is smaller, the amplitude of δx_e and c_{x_e} will become smaller. This is the qualitative feature that can be seen in Figs. 2 and 7.

For c_T on the other hand, the scale dependence changes it in the opposite manner—scales in which $\mathcal{T}_{b/c}(k, z)$ is smaller lead to a higher c_T . This counterintuitive behavior can be traced back to Eq. (13); the terms in the second and the third rows, which tend to decrease the value of c_T , are now smaller.³ Thus, even though the source term which drives c_T to higher values is also decreased, c_T is increased compared to the scale-free analysis. Specifically, for $k = 0.3 \text{ Mpc}^{-1}$ we find the following linear fit:

$$c_T(k = 0.3 \text{ Mpc}^{-1}, z) \approx 0.46 - 0.0044(z - 35). \quad (30)$$

IV. THE 21-CM SIGNAL DURING DARK AGES

Because 21cmFirstCLASS can be initialized at recombination, it can be used to calculate $\Delta_{21}^2(k, z)$ both in the

³Although $\mathcal{D}_b(k, z)$ appears both in the numerator and in the denominator of Eq. (13), the impact of $\mathcal{T}_{b/c}(k, z)$ in the numerator is stronger. This is because the numerator is inside the integral and thus suffers more suppression from high redshifts.

nonlinear cosmic dawn epoch, like 21cmFAST, and in the dark ages. During the dark ages, the fluctuations are expected to be small, and linear perturbation theory can be applied.⁴ This approach was taken in LC07, where the fully relativistic Boltzmann equations were solved. In order to test the output of 21cmFirstCLASS and compare with their work, we rederive the expressions for the linear brightness temperature fluctuations, but in a more tractable way. We do this step by step and identify the most dominant terms. In the derivation we present below, we make some simplifying assumptions that help us to get a nice, short, approximated expression for the 21-cm fluctuations, Eq. (43). Our full derivation, where these assumptions are relaxed, can be found in Appendixes B and C. The only differences between our full derivation and the derivation of LC07 are that (1) we ignore CMB temperature fluctuations, i.e., we assume $T_\gamma = \bar{T}_\gamma$ as fluctuations in the CMB temperature are much smaller than δ_b on subhorizon scales after decoupling; and (2) we ignore derivatives in the gravitational potential, which is justified during matter domination [84,85].

First, let us assume for simplicity that there are no fluctuations in T_k and x_e , i.e., $\delta T_k = \delta x_e = 0$. This assumption is justified, at least at low redshifts, because we know from Fig. 5 that the fluctuations in these fields barely change the 21-cm power spectrum at the end of the dark ages, at $z \sim 35$. We will shortly understand why. Since $\bar{x}_{\text{coll}} \propto \rho_b$, under these assumptions we have $\delta x_{\text{coll}}/\bar{x}_{\text{coll}} = \delta_b$. Before cosmic dawn, the spin temperature is given simply by

$$T_s = \frac{x_{\text{CMB}} + x_{\text{coll}}}{x_{\text{CMB}}/T_\gamma + x_{\text{coll}}/T_k}, \quad (31)$$

and thus the fractional fluctuation in the spin temperature, in linear theory, is

$$\frac{\delta T_s}{\bar{T}_s} = -\frac{(1 - \bar{T}_k/T_\gamma)\bar{x}_{\text{coll}}\bar{x}_{\text{CMB}}}{(\bar{x}_{\text{CMB}} + \bar{x}_{\text{coll}})(\bar{x}_{\text{CMB}}\bar{T}_k/T_\gamma + \bar{x}_{\text{coll}})}\delta_b. \quad (32)$$

The minus sign on the rhs of Eq. (32) makes sense, as in overdense regions collisions are more efficient and the spin temperature is driven to lower values.

In the limit $\tau_{21} \ll 1$, the brightness temperature is

$$T_{21} \propto (1 - x_e)n_{\text{H}} \left(1 - \frac{T_\gamma}{T_s}\right) \left(1 + \frac{1}{H} \frac{d(\hat{\mathbf{n}} \cdot \mathbf{v}_b)}{d(\hat{\mathbf{n}} \cdot \mathbf{x})}\right)^{-1}, \quad (33)$$

where the factor of proportionality contains terms that are uniform in space. Assuming $\delta x_e = 0$, we then find that the fractional fluctuation in the brightness temperature in linear theory is

$$\delta_{21} \equiv \frac{\delta T_{21}}{\bar{T}_{21}} = \delta_b - \frac{\delta T_s}{\bar{T}_s} \frac{1}{1 - \bar{T}_s/T_\gamma} - \frac{1}{H} \frac{d(\hat{\mathbf{n}} \cdot \mathbf{v}_b)}{d(\hat{\mathbf{n}} \cdot \mathbf{x})}. \quad (34)$$

Then, using Eqs. (31), (32), and (34), it is straightforward to show that

$$\delta_{21} \equiv c_{21,\text{iso}}\delta_b - \frac{1}{H} \frac{d(\hat{\mathbf{n}} \cdot \mathbf{v}_b)}{d(\hat{\mathbf{n}} \cdot \mathbf{x})}, \quad (35)$$

where

$$c_{21,\text{iso}} = \frac{2\bar{x}_{\text{CMB}} + \bar{x}_{\text{coll}}}{\bar{x}_{\text{CMB}} + \bar{x}_{\text{coll}}}. \quad (36)$$

The physical meaning of $c_{21,\text{iso}}$ is the ratio between δ_{21} and δ_b in the absence of peculiar velocity which introduces anisotropies in δ_{21} (see below). From the very simple expression of Eq. (36), we see that overdense regions lead to a stronger 21-cm signal, as expected. Moreover, the fluctuations in the signal grow in time, not only because δ_b grows, but also because $c_{21,\text{iso}}$ grows; initially, $\bar{x}_{\text{coll}} \gg \bar{x}_{\text{CMB}} \approx 1$ and $c_{21,\text{iso}} \rightarrow 1$, but at late times $\bar{x}_{\text{coll}} \ll \bar{x}_{\text{CMB}} \approx 1$ and $c_{21,\text{iso}} \rightarrow 2$.

Equation (35) is a relation in real space. In Fourier space, we know from the continuity equation (assuming matter domination, when the gravitational potential was constant) that

$$\begin{aligned} \hat{\mathbf{n}} \cdot \mathbf{v}_b &= i \frac{\hat{\mathbf{n}} \cdot \mathbf{k}}{k^2} \frac{d\delta_b}{dt} = i \frac{\hat{\mathbf{n}} \cdot \mathbf{k}}{k^2} \frac{dz}{dt} \frac{d\delta_b}{dz} \\ &= -iH \frac{\hat{\mathbf{n}} \cdot \mathbf{k}}{k^2} \frac{d \ln \mathcal{T}_b(k, z)}{d \ln(1+z)} \delta_b, \end{aligned} \quad (37)$$

and thus in Fourier space Eq. (35) becomes

$$\delta_{21} = \left[c_{21,\text{iso}} - \frac{(\hat{\mathbf{n}} \cdot \mathbf{k})^2}{k^2} \frac{d \ln \mathcal{T}_b(k, z)}{d \ln(1+z)} \right] \delta_b. \quad (38)$$

From here, we see that the peculiar velocity results in $c_{21} \equiv \delta_{21}/\delta_b$, which is not only scale-dependent, but also nonisotropic due to the line-of-sight effect. The 21-cm *anisotropic* power spectrum can then be given in terms of the primordial curvature power spectrum $\Delta_{\mathcal{R}}^2(k) = A_s(k/k_\star)^{n_s-1}$,

$$\begin{aligned} \Delta_{21}^2(k, \mu, z) &= \Delta_{\mathcal{R}}^2(k) \bar{T}_{21}^2(z) c_{21,\text{iso}}^2(k, z) \mathcal{T}_b^2(k, z) \\ &\times \left[1 - \mu^2 c_{21,\text{iso}}^{-1} \frac{d \ln \mathcal{T}_b(k, z)}{d \ln(1+z)} \right]^2, \end{aligned} \quad (39)$$

where $\mu \equiv (\hat{\mathbf{n}} \cdot \mathbf{k})/k$. Finally, the *isotropic* (or angle-averaged) 21-cm power spectrum is

⁴Though nonlinear effects can contribute at the few-percent level [67,76].

$$\begin{aligned}
 \Delta_{21}^2(k, z) &= \frac{1}{4\pi} \int d\Omega \Delta_{21}^2(k, \mu, z) \\
 &= \frac{1}{2} \int_{-1}^1 d\mu \Delta_{21}^2(k, \mu, z) \\
 &= \Delta_{\mathcal{R}}^2(k) \bar{T}_{21}^2(z) c_{21,\text{iso}}^2(k, z) \mathcal{T}_b^2(k, z) \\
 &\quad \times \left[1 - \frac{2}{3} c_{21,\text{iso}}^{-1} \frac{d \ln \mathcal{T}_b(k, z)}{d \ln(1+z)} \right. \\
 &\quad \left. + \frac{1}{5} c_{21,\text{iso}}^{-2} \left(\frac{d \ln \mathcal{T}_b(k, z)}{d \ln(1+z)} \right)^2 \right]. \quad (40)
 \end{aligned}$$

In the last equality of Eq. (40), the term in front of the square brackets can be viewed as the 21-cm power spectrum in the absence of peculiar velocity, while the term inside the square brackets represents its contribution. Let us estimate the logarithmic derivative of $\mathcal{T}_b(k, z)$ that appears in the square brackets,

$$\begin{aligned}
 \frac{d \ln \mathcal{T}_b(k, z)}{d \ln(1+z)} &= \frac{d \ln \mathcal{T}_c(k, z)}{d \ln(1+z)} + \frac{d \ln \mathcal{T}_{b/c}(k, z)}{d \ln(1+z)} \\
 &= -1 + \frac{d \ln \mathcal{T}_{b/c}(k, z)}{d \ln(1+z)} < 0, \quad (41)
 \end{aligned}$$

where the second equality follows $\mathcal{T}_c(k, z) \propto D(z) \propto (1+z)^{-1}$ and the inequality is due to the fact that the slope of $\mathcal{T}_{b/c}(k, z)$ is nonpositive; from Fig. 2 we see that this derivative is almost zero at low redshifts, while at high redshifts it can be $\mathcal{O}(-10)$. Thus, we see from Eqs. (40) and (41) that the peculiar velocity tends to add power to the 21-cm signal. If we ignore the logarithmic derivative of $\mathcal{T}_{b/c}(k, z)$ and adopt the expression for $c_{21,\text{iso}}$ from Eq. (36), then we see from Eq. (40) that at high redshifts the peculiar velocity enhances $\Delta_{21}^2(k, z)$ by a factor of $1 + \frac{2}{3} + \frac{1}{5} = \frac{28}{15} = 1.87$ [21,67,86], while at low redshifts it enhances $\Delta_{21}^2(k, z)$ by a factor of $1 + \frac{1}{3} + \frac{1}{20} = \frac{83}{60} = 1.38$.

Although Eq. (40) is theoretically correct,⁵ the expression we derived for $c_{21,\text{iso}}$ in Eq. (36) is too simplistic and lacks the contribution of fluctuations in T_k and x_e . Once these fluctuations are taken into account, the expression for $c_{21,\text{iso}}$ becomes (still assuming $\tau_{21} \ll 1$, see details in Appendix B)

$$\begin{aligned}
 c_{21,\text{iso}}(k, z) &= \frac{2\bar{x}_{\text{CMB}} + \bar{x}_{\text{coll}}}{\bar{x}_{\text{CMB}} + \bar{x}_{\text{coll}}} + \left[\frac{\bar{x}_{\text{CMB}} \bar{C}_{10}^{-1} \bar{n}_{\text{H}} \bar{x}_e}{\bar{x}_{\text{CMB}} + \bar{x}_{\text{coll}}} (f_{\text{H}}^{-1} \bar{\kappa}_{1-0}^{\text{eH}} + \bar{\kappa}_{1-0}^{\text{pH}} - \bar{\kappa}_{1-0}^{\text{HH}}) + \frac{\bar{x}_e}{1 - \bar{x}_e} \right] c_{x_e}(k, z) \\
 &\quad + \left[\frac{\bar{x}_{\text{CMB}} \bar{C}_{10}^{-1} \bar{n}_{\text{H}} \bar{T}_k}{\bar{x}_{\text{CMB}} + \bar{x}_{\text{coll}}} \left((1 - \bar{x}_e) \frac{\partial \bar{\kappa}_{1-0}^{\text{HH}}}{\partial \bar{T}_k} + f_{\text{H}}^{-1} \bar{x}_e \frac{\partial \bar{\kappa}_{1-0}^{\text{eH}}}{\partial \bar{T}_k} + \bar{x}_e \frac{\partial \bar{\kappa}_{1-0}^{\text{pH}}}{\partial \bar{T}_k} \right) - \frac{1}{1 - \bar{T}_k/T_\gamma} \right] c_T(k, z). \quad (42)
 \end{aligned}$$

Note that since c_T and c_{x_e} are scale-dependent quantities, so too is $c_{21,\text{iso}}$. In addition, note that the contribution of c_{x_e} to $c_{21,\text{iso}}$ is proportional to \bar{x}_e , which is very small between recombination and reionization, and we can therefore take the approximation $\bar{x}_e \approx 0$ in Eq. (42),

$$\begin{aligned}
 c_{21,\text{iso}}(k, z) &\approx \frac{2\bar{x}_{\text{CMB}} + \bar{x}_{\text{coll}}}{\bar{x}_{\text{CMB}} + \bar{x}_{\text{coll}}} \\
 &\quad + \left[\frac{\bar{x}_{\text{CMB}}}{\bar{x}_{\text{CMB}} + \bar{x}_{\text{coll}}} \frac{\partial \ln \bar{\kappa}_{1-0}^{\text{HH}}}{\partial \ln \bar{T}_k} - \frac{1}{1 - \bar{T}_k/T_\gamma} \right] c_T(k, z). \quad (43)
 \end{aligned}$$

Although this expression may still appear rather simplistic, we stress that it results in only a subpercent error below $z \lesssim 80$ (above this redshift, corrections from the optical depth become more important, but are still not very significant, see Fig. 8). Together with Eqs. (39)–(41), it can therefore be used to gain insight as to how the 21-cm power spectrum behaves during the dark ages.

Notice that if the expression in the square brackets of Eq. (43) vanishes, then $c_{21,\text{iso}}$ does not depend on early temperature fluctuations, and it becomes completely scale

independent. We find that the special redshift where that happens is $z \approx 37$. This explains why the power spectrum in 21cmFAST is not very sensitive to early temperature fluctuations at the vicinity of $z = 35$, as was demonstrated in Fig. 5. At lower redshifts, the weight of c_T becomes positive and larger, and since its evolution depends on its past values, the initial conditions at $z = 35$ carry more importance, until the nonlinearities of the SFRD dominate the power spectrum.

In Fig. 8 we show how each of the lines in Eq. (42) contributes to $c_{21,\text{iso}}(z)$, including the $\mathcal{O}(\tau_{21})$ term that we have neglected above, while taking the scale-independent quantities of $c_T(z)$ and $c_{x_e}(z)$. As expected, the crude approximation of Eq. (36) works well at low redshifts, at $z \sim 35$. The c_{x_e} correction barely modifies $c_{21,\text{iso}}$, while the c_T correction modifies $c_{21,\text{iso}}$ by $\sim 30\%$ at $z \sim 100$ and its impact becomes smaller toward lower redshifts. The τ_{21} correction is mainly important at high redshifts, $z \gtrsim 100$ ($\bar{\tau}_{21}$ monotonically decreases from ~ 0.08 at $z \sim 700$ to ~ 0.02 at $z \sim 35$). We note that we cut Fig. 8 at $z = 300$

⁵Neglecting $\mathcal{O}(\tau_{21})$ corrections in the square brackets, see Appendixes B and C.

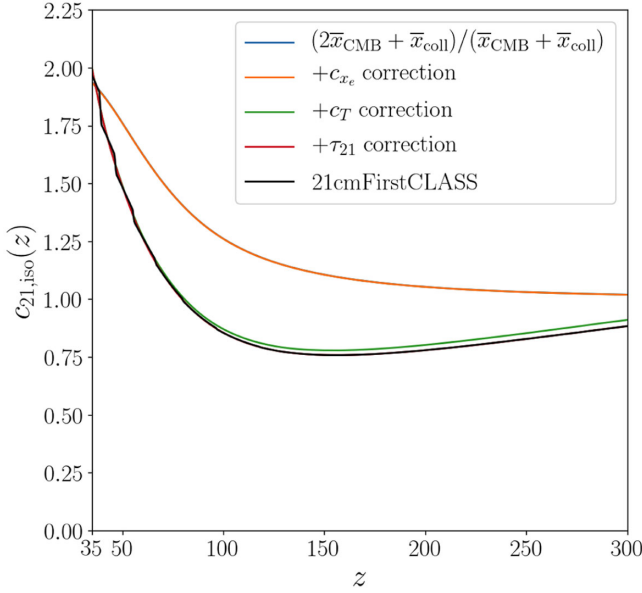


FIG. 8. The scale-independent $c_{21,\text{iso}}(z)$. The blue curve shows our crude approximation, Eq. (36). The orange curve shows the contribution from early ionization fluctuations, the first and the second rows in Eq. (42), and it completely overlaps with the blue curve. The green curve shows the contribution from early temperature fluctuations, which is achieved by considering all the rows in Eq. (42), or alternatively via Eq. (43) with excellent precision. The red curve shows the contribution from τ_{21} fluctuations, see details in Appendixes B and C. The black curve shows the redshift-dependent median of the $c_{21}(\mathbf{x}, z)$ box in 21cmFirstCLASS (when the peculiar velocity and HyRec are turned off) and it completely overlaps with the red curve at high redshifts. At low redshifts, the jagged artifact is the result of the linear interpolation used in 21cmFAST, see text for more details.

because of a theoretical uncertainty arising from the last term in Eq. (43); while we know that c_T becomes very small at high redshifts, this is the regime where $\bar{T}_k \rightarrow T_\gamma$ and it is not clear which one approaches zero more quickly, the numerator or the denominator.

As a sanity check, we also plot in Fig. 8 the median of the $c_{21}(\mathbf{x}, z)$ box in 21cmFirstCLASS. For this test we have turned off the peculiar velocity in 21cmFAST such that $c_{21} \equiv c_{\text{iso},21}$. We see again that the agreement between 21cmFirstCLASS and the linear scale-independent theory is excellent at high redshifts. Below $z \sim 80$ the black curve becomes jagged. This feature is of course unphysical and it is the result of the evaluation of $\kappa_{1-0}^{\text{HH}}(T_k)$ in 21cmFAST. This quantity (as well as κ_{1-0}^{pH} and κ_{1-0}^{eH}) is *linearly* interpolated from an external table. According to Eq. (43), the derivative of κ_{1-0}^{HH} with respect to T_k has to be considered, and thus the jagged artifact⁶ is the

⁶In Fig. 8 we have evaluated all the colorful curves by using `scipy`'s interpolation function with a cubic interpolation scheme [87]. We have replicated the jagged artifact shown in the black curve by using instead a linear interpolation scheme.

consequence of 21cmFirstCLASS evaluating $\delta\kappa_{1-0}^{\text{HH}}/\delta T_k$ from a piecewise linear function. Because this artifact has no effect on the results shown in this paper, we defer its fix for future work.

V. NONLINEARITIES

Unlike the linear Boltzmann solver CAMB, 21cmFirstCLASS can take into account nonlinear fluctuations that arise from nonlinear growth of the density field. Below we outline the Lagrangian perturbation theory [88–94] scheme used in 21cmFAST to evolve the density field nonlinearly, but we generalize our formulas to account for scale-dependent growth.

The basic idea is to relate the initial (comoving) Lagrangian coordinates \mathbf{x} of the density field, evaluated linearly at some high redshift z_0 with the Eulerian coordinates \mathbf{x}_E of the density field at a lower redshift z . These two coordinates are related by the displacement field vector $\boldsymbol{\psi}(\mathbf{x}, z)$,

$$\mathbf{x}_E(\mathbf{x}, z) = \mathbf{x}(z_0) + \boldsymbol{\psi}(\mathbf{x}, z). \quad (44)$$

The information encoded in $\boldsymbol{\psi}(\mathbf{x}, z)$ maps the spatial displacement between redshift z_0 and redshift z of a mass located initially at coordinate \mathbf{x} . Knowing the value of $\boldsymbol{\psi}(\mathbf{x}, z)$ then allows one to coherently add masses together at \mathbf{x}_E , resulting in nonlinear fluctuations at sufficiently low redshifts. By construction, the time derivative of $\boldsymbol{\psi}(\mathbf{x}, z)$ is the velocity field, $\dot{\boldsymbol{\psi}}(\mathbf{x}, z) = \dot{\mathbf{x}}_E(\mathbf{x}, z) = \mathbf{v}_b(\mathbf{x}, z)$, where we use the subscript b to emphasize that we are focusing on the baryon velocity. In the Zel'dovich approximation [95–97], the velocity of the baryons can be expressed with the baryon-density contrast δ_b via the continuity equation, which in Fourier space reads [98–100]

$$\mathbf{v}_b(\mathbf{k}, z) = \frac{i\mathbf{k}}{k^2} \delta_b(\mathbf{k}, z) = \frac{i\mathbf{k}}{k^2} \dot{\mathcal{D}}_b(k, z) \delta_0(\mathbf{k}). \quad (45)$$

Thus, in the Zel'dovich approximation, the displacement field vector in Fourier space is given by

$$\boldsymbol{\psi}(\mathbf{k}, z) = \frac{i\mathbf{k}}{k^2} [\mathcal{D}_b(k, z) - \mathcal{D}_b(k, z_0)] \delta_0(\mathbf{k}). \quad (46)$$

Note that, unlike the scale-independent scenario, here $\boldsymbol{\psi}(\mathbf{k}, z)$ cannot be separated into its spatial and temporal components.

Despite the fact that the Zel'dovich approximation correctly reproduces the linear growth of density and velocity perturbations, it fails to conserve momentum in the nonlinear regime. Therefore, second-order Lagrangian perturbation theory (2LPT) is implemented in 21cmFAST. The basic equations of 2LPT can be found in Appendix D of Ref. [101] and the references therein. These equations

are expressed in terms of the scale-independent growth factor $D(z)$, and the scale dependence can be accounted for by replacing $D(z)$ with $\mathcal{D}_b(k, z)$, as we did above for the Zel'dovich approximation.

For the time being, as we have yet to incorporate the scale-dependent growth factor $\mathcal{D}_b(k, z)$ in `21cmFirstCLASS`, we can currently study how the nonlinear evolution scheme of 2LPT modifies the analytical results we previously obtained for the scale-independent scenario. In that context, we have already seen in Fig. 5 the effect of nonlinearities at low redshifts on the 21-cm power spectrum. On large scales ($k = 0.1 \text{ Mpc}^{-1}$) nonlinearities enhance the power spectrum by $\mathcal{O}(100\%)$ at $z \sim 7$, while on small scales ($k = 0.5 \text{ Mpc}^{-1}$) they suppress the power spectrum by $\mathcal{O}(25\%)$. This will be revisited in follow-up work.

VI. COMPARISON WITH CAMB

So far, we have compared our scale-independent linear theory with `21cmFirstCLASS` and we have generalized the equations to account for scale-dependent growth by simply replacing $D(z)$ with $\mathcal{D}_b(k, z)$. The key question that emerges now is the following: once scale-dependent growth is implemented in `21cmFirstCLASS`, will it be able to predict the 21-cm anisotropies during the dark ages?

Currently, the code that computes the linear 21-cm anisotropies during the dark ages most comprehensively is `CAMB`. Similarly to `CLASS`, this code solves the fully relativistic coupled Boltzmann and Einstein equations for the linear scale-dependent perturbations in the density, velocity, and temperature fields. Once `CAMB` has evaluated these perturbations, it can compute the fluctuations in the spin temperature and the brightness temperature with very similar equations to those derived in Sec. IV (except that `CAMB` also accounts for fluctuations in the CMB temperature and does not ignore the small impact of gravitational fields, see more details in LC07).

Because the scale-dependent formalism we developed in this work is less rigorous than what `CAMB` does, it is not *a priori* clear that our formalism gives the correct results. We therefore present a comparison with `CAMB` in Fig. 9 for a wide range of scales between $35 \leq z \leq 100$. The vertical dashed curves represent the wave numbers associated with the horizon scale (times 10) and the Jeans scale (divided by 10). In the intermediate scales that span between these lines the comparison is very successful; for $z \leq 40, 50, 100$ the relative error is less than 0.5%, 1%, 5%, respectively. As expected, our formalism fails to predict the 21-cm anisotropies on superhorizon scales, since we have neglected in our equations the fluctuations in the CMB temperature. On scales smaller than the Jeans scale, the discrepancy is less severe, but still exists

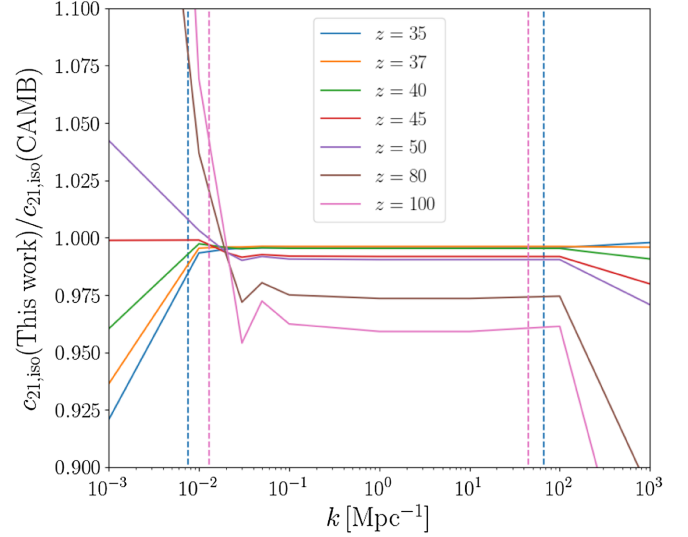


FIG. 9. Comparison of the scale-dependent $c_{21,\text{iso}}(k, z)$ between the formalism developed in this work and `CAMB`, as a function of wave number, for various redshifts. The vertical dashed curves represent the wave numbers associated with the horizon scale (times 10) and the Jeans scale (divided by 10).

because at these small scales the evolution equations of δ_b and δT_k are coupled [102,103], and we cannot simply take $\mathcal{D}_b(k, z)$ from `CLASS` to emulate the evolution of the baryon-density field. Plus, Jeans suppression causes δ_b to approach δ_γ , the density contrast of the CMB photons which we have neglected.

A very nice feature that can be seen in Fig. 9 is that, on subhorizon scales, the relative error is constant at $z = 37$, confirming our discussion below Eq. (43) that $c_{21,\text{iso}}$ becomes scale independent at this special redshift. Another feature that can be noticed is that the relative error increases with redshift. We suspect that the origin of this feature is that `CAMB` does not only evaluate the fluctuations differently than us, it also computes the background quantities differently. For example, throughout this paper we have assumed that the spin temperature is given by its expression in equilibrium, Eq. (3). Yet, `CAMB` solves the Boltzmann equation for the background spin temperature, Eq. (28) in LC07, thereby accounting for out-of-equilibrium effects in the spin temperature.

All this notwithstanding, it is important to realize that once the scale dependence is implemented in `21cmFirstCLASS`, we still should not expect it to match `CAMB` with less than a few-percent difference. As was discussed at the end of Sec. III A, `21cmFirstCLASS` works with the more precise recombination model of `HyRec`, while `CAMB` works with `RECFAST`. As we demonstrated in Fig. 3, the different recombination models lead to a relative difference of $\sim 4\%$ in c_T at $z = 100$, and according to Fig. 8, the weight of c_T in determining $c_{21,\text{iso}}$ becomes important at that redshift.

Moreover, `21cmFirstCLASS` includes two effects⁷ that `CAMB` does not in the evaluation of $\Delta_{21}^2(k, z)$; both of them were first included in `21cmFAST` in Ref. [106]. The first one is redshift space distortions (RSDs). The peculiar velocity impacts the brightness temperature in two ways. First, local peculiar velocity gradients modify the amplitude of the brightness temperature [this effect is already included in `CAMB` and is captured by our Eqs. (1) and (2)]. And second, because observations are performed in redshift space rather than real space, the signal shifts from real space coordinates \mathbf{x} to redshift space coordinates \mathbf{s} via $\mathbf{s} = \mathbf{x} + \hat{\mathbf{n}}(\hat{\mathbf{n}} \cdot \mathbf{v}_b)/H$ [21,76,86]. In order to simulate this effect, cells in the `BOX` of `21cmFAST` are shifted accordingly. The second effect that is already accounted in `21cmFirstCLASS` is the light cone effect [107–114]—measurements of modes parallel to the line of sight probe the brightness temperature at different redshifts. The light cone effect is addressed in `21cmFAST` by building the light cone box from interpolating adjacent coeval boxes (the latter are boxes for which all their cells correspond to a single redshift) along the line of sight. The RSD is a nonlinear effect and is beyond the scope of this work (but see analytical treatment in Refs. [76,86]). The light cone effect is even more challenging to analytically model as it mixes between time and space coordinates (but see an analytical estimate of the effect at the beginning of reionization in Ref. [107]). We thus leave a more thorough comparison with `CAMB` for future work, once the scale dependence is implemented in `21cmFirstCLASS`.

VII. CONCLUSIONS

The 21-cm signal is expected to provide a new window to the thermal and ionization states of the high-redshift Universe. The rich information in that signal, especially in its anisotropies pattern, cannot be utilized without having robust theoretical models. There are two important epochs in the history of the signal, each of which is modeled nowadays by a different theoretical framework. During the dark ages, above $z \sim 35$, the fluctuations in the signal are expected to be linear, hence they can be evolved via linear perturbation theory. This is what the `CAMB` code does rigorously, by solving the full Einstein-Boltzmann equations for all the linear fluctuations. At low redshifts, below $z \sim 35$, nonlinearities due to structure formation become important and seminumerical codes, like `21cmFAST`, are required for studying the vast cosmological and astrophysical parameter space.

⁷Another effect, which is absent in both `21cmFirstCLASS` and `CAMB`, is the inclusion of supersonic relative velocity between baryons and CDM [103–105]. This is a nonlinear effect arising from very small scales ($k \gtrsim 100 \text{ Mpc}^{-1}$) and can enhance the 21-cm power spectrum at the relevant scales ($0.005 \lesssim k \lesssim 1 \text{ Mpc}^{-1}$) by a few percent [76].

In the preceding article [62], we introduced our new code, `21cmFirstCLASS`. As an extension to `21cmFAST`, it is automatically able to calculate the 21-cm power spectrum during the nonlinear cosmic dawn epoch. To test the output of our code, we have developed here a new analytical framework to predict the linear contribution to the brightness temperature anisotropies. We first showed that initializing the evolution at recombination can lead to differences at the $\mathcal{O}(20\%)$ level in the cosmic dawn signal compared to the standard `21cmFAST` result.

In addition, the equations we derived indicate that `21cmFAST` overpredicts the brightness temperature fluctuations at $z \gtrsim 20$ by as much as $\mathcal{O}(10\%)$, which leads to a $\mathcal{O}(20\%)$ error in the 21-cm power spectrum at these redshifts. This arises because of a basic underlying assumption in `21cmFAST`, that the densities of baryons and cold dark matter are the same, i.e., $\delta_b = \delta_c$.

We then proposed an elegant solution to this problem: simply replace the scale-independent growth factor $D(z)$ with the scale-dependent growth factor $\mathcal{D}_b(k, z)$. Then, instead of solving dozens of coupled differential equations like `CAMB`, only two are required, one for δT_k and one for δx_e . These two equations are given in Eqs. (16)–(22) [along with Eqs. (A7)–(A9) to account for Peebles fluctuations], and their analytical solution is given by Eq. (23). For the brightness temperature fluctuations, only the early fluctuations in T_k matter, and we have managed to derive a simple analytical formula for $c_{21,\text{iso}} \equiv \delta_{21}/\delta_b$ (defined without the contribution of the peculiar velocity), Eq. (43), that works particularly well below $z \lesssim 80$. This equation can then be used alongside Eqs. (39) and (40) in the evaluation of the 21-cm dark ages power spectrum.

As a by-product of this work, we have found that at $z \approx 37$ the 21-cm power spectrum becomes scale independent and completely independent from the history of temperature fluctuations. Below that redshift, temperature fluctuations can matter in the evolution of the brightness temperature fluctuations, as mentioned above. Their weight at redshifts $25 \lesssim z \lesssim 35$ is still small, however, explaining why `21cmFirstCLASS`, as well as the fit of JBM23, yields only a $\sim 10\%$ difference there.

In order to verify that the formalism we have developed can be incorporated in the future in `21cmFirstCLASS` for predicting $\Delta_{21}^2(k, z)$ at the dark ages with a good precision level, our strategy was the following (see Fig. 1): First, we compared between the scale-independent theory and `21cmFirstCLASS`. The results of this comparison, shown in Fig. 8, are excellent; `21cmFirstCLASS` does exactly what it was designed to do (except for the jagged artifact at low redshifts which can be easily fixed in future versions of the code). And second, we compared between the scale-dependent theory and `CAMB`. The results of this comparison are presented in Fig. 9. At the scales of interest for 21-cm interferometers, between the horizon and the Jeans scale, our formalism appears to be robust, and there is only a

subpercent discrepancy with CAMB at $z \leq 50$ over a wide dynamic range of scales. As was discussed above, in the end, few-percent differences between 21cmFirstCLASS and CAMB are unavoidable because of the different recombination models used by the two codes, as well as other effects that are accounted for in 21cmFirstCLASS but not in CAMB (nonlinearities in the density field, RSD, and the light cone effect).

We are therefore optimistic that our formalism can be incorporated in 21cmFirstCLASS, making its upcoming public release a desirable code for studying the 21-cm anisotropies not only at cosmic dawn, but also during the dark ages. Its greatest strength, though, will be in the study of nonlinear models, as we demonstrate in Paper I [62]. 21cmFirstCLASS is thus poised to become a widely used tool for cosmological simulations of Λ CDM and beyond.

The supporting codes for this paper are openly available from the GitHub repository [115–119].

ACKNOWLEDGMENTS

We thank Julian B. Muñoz for useful discussions. We also acknowledge the efforts of the 21cmFAST and CLASS and CAMB authors to produce state-of-the-art public 21-cm and CMB codes. J. F. is supported by the Zin fellowship awarded by the BGU Kreitmann School. E. D. K. acknowledges support from an Azrieli faculty fellowship. E. D. K. also acknowledges joint support from the U.S.-Israel Binational Science Foundation (BSF, Grant No. 2022743) and the U.S. National Science Foundation (NSF, grant No. 2307354), and support from the ISF-NSFC joint research program (grant No. 3156/23).

APPENDIX A: PEEBLES FLUCTUATIONS

The Peebles coefficient in Eq. (6) represents the probability that a hydrogen atom in the first excited state reaches the ground state before being ionized. It is given by [75,84,85]

$$\mathcal{C} = \frac{\Lambda_\alpha + \Lambda_{2\gamma}}{\Lambda_\alpha + \Lambda_{2\gamma} + \beta_{\text{ion}}^{(2)}}, \quad (\text{A1})$$

where $\Lambda_{2\gamma} = 8.227 \text{ sec}^{-1}$ is the two-photon decay rate from the $2s$ level to the $1s$ level, Λ_α is the resonance escape of Ly α photons,

$$\Lambda_\alpha = \frac{8\pi H}{\lambda_\alpha^3 n_{\text{H}}(1 - x_e)}, \quad (\text{A2})$$

where $\lambda_\alpha = 121.6 \text{ nm}$ is the Ly α wavelength, and the photoionization rate from the first excited state is given by

$$\beta_{\text{ion}}^{(2)} = \beta_{\text{ion}} e^{3\epsilon_0/(4k_B T_\gamma)} = \alpha_{\text{rec}} \left(\frac{m_e k_B T_\gamma}{2\pi \hbar^2} \right)^{3/2} e^{-\epsilon_0/(4k_B T_\gamma)}. \quad (\text{A3})$$

Applying linear perturbation theory on Eq. (A1), one finds that

$$\frac{\delta \mathcal{C}}{\mathcal{C}} = \bar{\mathcal{C}} \frac{\bar{\beta}_{\text{ion}}^{(2)}}{\bar{\Lambda}_\alpha + \bar{\Lambda}_{2\gamma}} \left(-\frac{\delta \beta_{\text{ion}}^{(2)}}{\bar{\beta}_{\text{ion}}^{(2)}} + \frac{\bar{\Lambda}_\alpha}{\bar{\Lambda}_\alpha + \bar{\Lambda}_{2\gamma}} \frac{\delta \Lambda_\alpha}{\bar{\Lambda}_\alpha} \right). \quad (\text{A4})$$

From Eqs. (A2) and (A3) we see that

$$\frac{\delta \Lambda_\alpha}{\bar{\Lambda}_\alpha} = -\delta_b + \frac{\delta x_e}{1 - \bar{x}_e}, \quad (\text{A5})$$

$$\frac{\delta \beta_{\text{ion}}^{(2)}}{\bar{\beta}_{\text{ion}}^{(2)}} = \frac{\delta \alpha_{\text{rec}}}{\bar{\alpha}_{\text{rec}}} = \frac{\partial \ln \alpha_B}{\partial \bar{T}_k} \delta T_k, \quad (\text{A6})$$

where we assumed $\alpha_{\text{rec}} \approx \alpha_B(T_k)$, just as in Sec. III. From Eqs. (15) and (16) and Eqs. (A4)–(A6) we see that the Peebles fluctuations modify the elements of the A and B matrices according to

$$A_{21} \rightarrow A_{21} - \bar{\mathcal{C}} \frac{\bar{\beta}_{\text{ion}}^{(2)}}{\bar{\Lambda}_\alpha + \bar{\Lambda}_{2\gamma}} \frac{\partial \ln \alpha_B}{\partial \bar{T}_k} \frac{d\bar{x}_e}{dz}, \quad (\text{A7})$$

$$A_{22} \rightarrow A_{22} + \bar{\mathcal{C}} \frac{\bar{\beta}_{\text{ion}}^{(2)}}{(\bar{\Lambda}_\alpha + \bar{\Lambda}_{2\gamma})^2} \frac{1}{1 - \bar{x}_e} \frac{d\bar{x}_e}{dz}, \quad (\text{A8})$$

$$B_2 \rightarrow B_2 - \bar{\mathcal{C}} \frac{\bar{\beta}_{\text{ion}}^{(2)}}{(\bar{\Lambda}_\alpha + \bar{\Lambda}_{2\gamma})^2} \frac{d\bar{x}_e}{dz} \mathcal{D}_b(k, z). \quad (\text{A9})$$

It should be noted that, in principle, Eq. (A5) is missing a term proportional to $\mathbf{k} \cdot \mathbf{v}_b$ [67,76,120], whose origin comes from modifications in Λ_α due to local peculiar velocities. It is justified, however, to discard this term in our analysis because (1) Peebles fluctuations only affect c_{x_e} at high redshift, leaving c_T unchanged, and (2) fluctuations in the brightness temperature are mostly determined by c_T , not c_{x_e} [see Eq. (43)].

APPENDIX B: BRIGHTNESS TEMPERATURE FLUCTUATIONS AT THE DARK AGES

In this appendix we derive the linear brightness temperature fluctuations during the dark ages. This is similar to the calculation presented in Sec. IV but here we relax the assumptions that were made in the main text. To make the calculation as tractable as possible, we begin by assuming $\tau_{21} \ll 1$, but let the temperature and ionization fraction fluctuate.

The collision coupling is given by $x_{\text{coll}} = T_\star C_{10}/(A_{10} T_\gamma)$, where $T_\star = 68.2 \text{ mK}$ is the hydrogen hyperfine energy gap (in units of mK), and

$$C_{10} = (1 - x_e) n_{\text{H}} \kappa_{1-0}^{\text{HH}} + x_e (n_{\text{H}} + n_{\text{He}}) \kappa_{1-0}^{\text{eH}} + x_e n_{\text{H}} \kappa_{1-0}^{\text{pH}}. \quad (\text{B1})$$

The κ_{1-0}^{iH} parameters are the collision rates (in units of cm^3/sec) of hydrogen atoms with particles of species i and

are functions of T_k only. In 21cmFAST, their tabulated values are taken from [121–123]. Thus, the fractional fluctuation in x_{coll} to linear order is

$$\frac{\delta x_{\text{coll}}}{\bar{x}_{\text{coll}}} = \delta_b + \bar{C}_{10}^{-1} \bar{n}_H \left\{ \left[f_H^{-1} \bar{\kappa}_{1-0}^{\text{eH}} + \bar{\kappa}_{1-0}^{\text{pH}} - \bar{\kappa}_{1-0}^{\text{HH}} \right] \delta x_e + \left[(1 - \bar{x}_e) \frac{\partial \bar{\kappa}_{1-0}^{\text{HH}}}{\partial \bar{T}_k} + f_H^{-1} \bar{x}_e \frac{\partial \bar{\kappa}_{1-0}^{\text{eH}}}{\partial \bar{T}_k} + \bar{x}_e \frac{\partial \bar{\kappa}_{1-0}^{\text{pH}}}{\partial \bar{T}_k} \right] \delta T_k \right\}, \quad (\text{B2})$$

where $f_H \equiv \bar{n}_H / (\bar{n}_H + \bar{n}_{\text{He}}) \approx 0.925$. Taking temperature fluctuations into account modifies Eq. (32),

$$\frac{\delta T_s}{\bar{T}_s} = - \frac{(1 - \bar{T}_k / T_\gamma) \bar{x}_{\text{coll}} \bar{x}_{\text{CMB}}}{(\bar{x}_{\text{CMB}} + \bar{x}_{\text{coll}}) (\bar{x}_{\text{CMB}} \bar{T}_k / T_\gamma + \bar{x}_{\text{coll}})} \frac{\delta x_{\text{coll}}}{\bar{x}_{\text{coll}}} + \frac{\bar{x}_{\text{coll}}}{\bar{x}_{\text{CMB}} \bar{T}_k / T_\gamma + \bar{x}_{\text{coll}}} \frac{\delta T_k}{\bar{T}_k}, \quad (\text{B3})$$

while taking ionization fluctuations into account modifies Eq. (34),

$$\delta_{21} = \delta_b - \frac{\delta T_s}{\bar{T}_s} \frac{1}{1 - \bar{T}_s / T_\gamma} - \frac{1}{H} \frac{d(\hat{\mathbf{n}} \cdot \mathbf{v}_b)}{d(\hat{\mathbf{n}} \cdot \mathbf{x})} + \frac{\delta x_e}{1 - \bar{x}_e}. \quad (\text{B4})$$

Then, combining Eqs. (B2)–(B4) and using the definitions of c_T , c_{x_e} , and $c_{21,\text{iso}}$ results in Eq. (42). We note that Eq. (B3) is consistent with Eq. (32) in LC07 when the small $\mathcal{O}(\tau_{21})$ term and CMB temperature fluctuations are ignored.

To account for the fluctuations in the optical depth, we need to modify Eq. (B3), as fluctuations in x_{CMB} contribute to the fluctuations in T_s ,

$$\frac{\delta T_s}{\bar{T}_s} \rightarrow \frac{\delta T_s}{\bar{T}_s} + \frac{(1 - \bar{T}_k / T_\gamma) \bar{x}_{\text{coll}} \bar{x}_{\text{CMB}}}{(\bar{x}_{\text{CMB}} + \bar{x}_{\text{coll}}) (\bar{x}_{\text{CMB}} \bar{T}_k / T_\gamma + \bar{x}_{\text{coll}})} \frac{\delta x_{\text{CMB}}}{\bar{x}_{\text{CMB}}}, \quad (\text{B5})$$

where to linear order,

$$\frac{\delta x_{\text{CMB}}}{\bar{x}_{\text{CMB}}} = \delta \left[\ln \left(\frac{1 - e^{-\tau_{21}}}{\tau_{21}} \right) \right] = \left(\frac{\bar{\tau}_{21}}{e^{\bar{\tau}_{21}} - 1} - 1 \right) \frac{\delta \tau_{21}}{\bar{\tau}_{21}}. \quad (\text{B6})$$

The fractional fluctuations in the optical depth $\delta \tau_{21} / \bar{\tau}_{21}$ are given by an expression very similar to Eq. (B4), but not exactly the same,

$$\frac{\delta \tau_{21}}{\bar{\tau}_{21}} = \delta_b - \frac{\delta T_s}{\bar{T}_s} - \frac{1}{H} \frac{d(\hat{\mathbf{n}} \cdot \mathbf{v}_b)}{d(\hat{\mathbf{n}} \cdot \mathbf{x})} + \frac{\delta x_e}{1 - \bar{x}_e}. \quad (\text{B7})$$

In addition, the assumption $\tau_{21} \ll 1$ in Eq. (33) has to be relaxed,

$$T_{21} \propto (1 - x_e) n_H \left(1 - \frac{T_\gamma}{T_s} \right) \left(1 + \frac{1}{H} \frac{d(\hat{\mathbf{n}} \cdot \mathbf{v}_b)}{d(\hat{\mathbf{n}} \cdot \mathbf{x})} \right)^{-1} \frac{1 - e^{-\tau_{21}}}{\tau_{21}}, \quad (\text{B8})$$

where again the factor of proportionality contains terms that are uniform in space. As a consequence, Eq. (B4) is modified,

$$\delta_{21} = \delta_b - \frac{\delta T_s}{\bar{T}_s} \frac{1}{1 - \bar{T}_s / T_\gamma} - \frac{1}{H} \frac{d(\hat{\mathbf{n}} \cdot \mathbf{v}_b)}{d(\hat{\mathbf{n}} \cdot \mathbf{x})} + \frac{\delta x_e}{1 - \bar{x}_e} + \delta \left[\ln \left(\frac{1 - e^{-\tau_{21}}}{\tau_{21}} \right) \right]. \quad (\text{B9})$$

It should be noted that Eqs. (B6)–(B9) are consistent with Eq. (22) in LC07.

Combining Eqs. (B6) and (B9) yields the following modification to δ_{21} :

$$\delta_{21} \rightarrow \delta_{21} + \left(\frac{\bar{\tau}_{21}}{e^{\bar{\tau}_{21}} - 1} - 1 \right) \frac{\delta \tau_{21}}{\bar{\tau}_{21}}. \quad (\text{B10})$$

Because of the peculiar velocity term in Eq. (B7), we need to modify our definition of $c_{21,\text{iso}}$ in Eq. (35),

$$\delta_{21} \equiv c_{21,\text{iso}} \delta_b - \frac{\bar{\tau}_{21}}{e^{\bar{\tau}_{21}} - 1} \frac{1}{H} \frac{d(\hat{\mathbf{n}} \cdot \mathbf{v}_b)}{d(\hat{\mathbf{n}} \cdot \mathbf{x})}. \quad (\text{B11})$$

It can be shown that $\delta \tau_{21} / (\bar{\tau}_{21} \cdot \delta_b)$ is positive (i.e., overdense regions lead to a stronger optical depth), and since the expression in the parentheses of Eq. (B10) can be Taylor expanded to $-\bar{\tau}_{21}/2$, we conclude that $c_{21,\text{iso}}$ receives a negative contribution from the optical depth (see Fig. 8). Also, we note that the factor $\bar{\tau}_{21} / (e^{\bar{\tau}_{21}} - 1) \sim 1 - \bar{\tau}_{21}/2$ has to be properly inserted into Eqs. (39) and (40) when the 21-cm power spectrum is evaluated.

APPENDIX C: DISENTANGLING T_s AND x_{CMB}

An inevitable challenge arises when attempting to calculate T_s in Eq. (31). It depends on x_{CMB} , while x_{CMB} depends on τ_{21} which depends on T_s . Therefore, T_s and x_{CMB} are mathematically entangled.

To overcome this difficulty numerically, we use the value of T_s from the previous iteration in calculating the current value of the optical depth. This is a very good approximation provided that the redshift step is small enough and T_s remains roughly the same between two consecutive redshift iterations (see another approach of solution by iterations in Refs. [71,124]). As for the initial value of T_s , we expand x_{CMB} to first order in τ_{21} ,

$$\begin{aligned} T_s &\approx \frac{1 - \frac{\tau_{21}}{2} + x_{\text{coll}}}{(1 - \frac{\tau_{21}}{2}) T_\gamma^{-1} + T_k^{-1} x_{\text{coll}}} \\ &\approx \frac{1 + x_{\text{coll}}}{T_\gamma^{-1} + T_k^{-1} x_{\text{coll}}} \\ &\quad - \frac{\tau_{21}}{2} \frac{(1 - T_k / T_\gamma) x_{\text{coll}}}{(T_\gamma^{-1} + T_k^{-1} x_{\text{coll}}) (T_k / T_\gamma + x_{\text{coll}})}. \end{aligned} \quad (\text{C1})$$

Using the zeroth order in τ_{21} , the solution to T_s can be written in the following form:

$$1 - \frac{T_s}{T_\gamma} = \frac{(1 - T_k/T_\gamma)x_{\text{coll}}}{T_k/T_\gamma + x_{\text{coll}}}. \quad (\text{C2})$$

Combining Eqs. (C1) and (C2), it follows that

$$T_s = \frac{1 + x_{\text{coll}}}{T_\gamma^{-1} + T_k^{-1}x_{\text{coll}}} - \frac{1}{2}\tau_{21}T_s \left(\frac{T_s^{-1}}{T_\gamma^{-1} + T_k^{-1}x_{\text{coll}}} - \frac{T_k/T_\gamma}{T_k/T_\gamma + x_{\text{coll}}} \right). \quad (\text{C3})$$

Now, using once again the zeroth-order solution to T_s in the rhs of Eq. (C3), we arrive at

$$\left(\frac{1}{1 - \bar{T}_s/T_\gamma} + \frac{\bar{x}_{\text{CMB}}F(\bar{\tau}_{21})}{\bar{x}_{\text{CMB}} + \bar{x}_{\text{coll}}} \right) \frac{\delta T_s}{\bar{T}_s} = - \frac{\bar{x}_{\text{CMB}}}{\bar{x}_{\text{CMB}} + \bar{x}_{\text{coll}}} \frac{\delta x_{\text{coll}}}{\bar{x}_{\text{coll}}} + \frac{1}{1 - \bar{T}_k/T_\gamma} \frac{\delta T_k}{\bar{T}_k} + \frac{\bar{x}_{\text{CMB}}F(\bar{\tau}_{21})}{\bar{x}_{\text{CMB}} + \bar{x}_{\text{coll}}} \left(\delta_b - \frac{1}{H} \frac{d(\hat{\mathbf{n}} \cdot \mathbf{v}_b)}{d(\hat{\mathbf{n}} \cdot \mathbf{x})} + \frac{\delta x_e}{1 - \bar{x}_e} \right), \quad (\text{C5})$$

where we have defined for brevity

$$F(\bar{\tau}_{21}) \equiv \frac{\bar{\tau}_{21}}{e^{\bar{\tau}_{21}} - 1} - 1 = -\frac{\bar{\tau}_{21}}{2} + \mathcal{O}(\bar{\tau}_{21}^2). \quad (\text{C6})$$

As a consistency check, note that Eq. (C5) reduces to Eq. (B3) in the limit $\bar{\tau}_{21} \rightarrow 0$. The above solution for δT_s can now be substituted in the expression for $\delta\tau_{21}$, Eq. (B7). In addition, because δT_s explicitly depends on the peculiar velocity, our definition of $c_{21,\text{iso}}$ has to be further modified,

$$T_s = \frac{1 + x_{\text{coll}}}{T_\gamma^{-1} + T_k^{-1}x_{\text{coll}}} - \frac{1}{2} \frac{\tau_{21}T_s(1 - T_k/T_\gamma)x_{\text{coll}}}{(T_k/T_\gamma + x_{\text{coll}})(1 + x_{\text{coll}})}. \quad (\text{C4})$$

It is worthwhile to note that Eq. (C4) is identical to Eq. (31) in LC07, thus their expression for T_s is the first-order solution in τ_{21} . Because $\tau_{21} \propto T_s^{-1}$, Eq. (C4) is a closed form solution to T_s , and we use it to set the initial value for T_s (which at recombination is $\approx T_\gamma$).

The mathematical entanglement of T_s and τ_{21} also poses another challenge when calculating their fluctuations analytically. From Eqs. (B5) and (B6), δT_s depends on $\delta\tau_{21}$, but from Eq. (B7) the latter depends on the former. Since we have two equations with two unknowns, the disentanglement is straightforward, although tedious,

$$\delta_{21} \equiv c_{21,\text{iso}}\delta_b - \frac{1}{H} \frac{d(\hat{\mathbf{n}} \cdot \mathbf{v}_b)}{d(\hat{\mathbf{n}} \cdot \mathbf{x})} \left[1 + F(\bar{\tau}_{21}) + \frac{\bar{x}_{\text{CMB}}F(\bar{\tau}_{21})}{\bar{x}_{\text{CMB}} + \bar{x}_{\text{coll}} + (1 - \bar{T}_s/T_\gamma)\bar{x}_{\text{CMB}}F(\bar{\tau}_{21})} \right], \quad (\text{C7})$$

and we stress that the expression in the brackets has to be accounted for when evaluating Eqs. (39) and (40).

-
- [1] P. Madau, A. Meiksin, and M. J. Rees, 21-CM tomography of the intergalactic medium at high redshift, *Astrophys. J.* **475**, 429 (1997).
 - [2] R. Barkana and A. Loeb, In the beginning: The first sources of light and the reionization of the Universe, *Phys. Rep.* **349**, 125 (2001).
 - [3] S. Bharadwaj and S. S. Ali, On using visibility correlations to probe the HI distribution from the dark ages to the present epoch. 1. Formalism and the expected signal, *Mon. Not. R. Astron. Soc.* **356**, 1519 (2005).
 - [4] S. Furlanetto, S. P. Oh, and F. Briggs, Cosmology at low frequencies: The 21 cm transition and the high-redshift Universe, *Phys. Rep.* **433**, 181 (2006).
 - [5] J. R. Pritchard and A. Loeb, 21-cm cosmology, *Rep. Prog. Phys.* **75**, 086901 (2012).
 - [6] A. Bera, R. Ghara, A. Chatterjee, K. K. Datta, and S. Samui, Studying cosmic dawn using redshifted HI 21-cm signal: A brief review, *J. Astrophys. Astron.* **44**, 10 (2023).
 - [7] A. K. Shaw *et al.*, Probing early Universe through redshifted 21-cm signal: Modeling and observational challenges, *J. Astrophys. Astron.* **44**, 4 (2023).
 - [8] R. Barkana and A. Loeb, Detecting the earliest galaxies through two new sources of 21 cm fluctuations, *Astrophys. J.* **626**, 1 (2005).
 - [9] S. Furlanetto, The global 21 centimeter background from high redshifts, *Mon. Not. R. Astron. Soc.* **371**, 867 (2006).
 - [10] J. Park, A. Mesinger, B. Greig, and N. Gillet, Inferring the astrophysics of reionization and cosmic dawn from galaxy luminosity functions and the 21-cm signal, *Mon. Not. R. Astron. Soc.* **484**, 933 (2019).
 - [11] J. B. Muñoz, C. Dvorkin, and F.-Y. Cyr-Racine, Probing the small-scale matter power spectrum with large-scale 21-cm data, *Phys. Rev. D* **101**, 063526 (2020).
 - [12] J. Park, N. Gillet, A. Mesinger, and B. Greig, Properties of reionization-era galaxies from JWST luminosity functions

- and 21-cm interferometry, *Mon. Not. R. Astron. Soc.* **491**, 3891 (2020).
- [13] B. Greig, A. Mesinger, and L. V. E. Koopmans, Reionization and cosmic dawn astrophysics from the square kilometre array: Impact of observing strategies, *Mon. Not. R. Astron. Soc.* **491**, 1398 (2020).
- [14] N. Thyagarajan *et al.*, Detection of cosmic structures using the bispectrum phase. II. First results from application to cosmic reionization using the hydrogen epoch of reionization array, *Phys. Rev. D* **102**, 022002 (2020).
- [15] Y. Qin, A. Mesinger, J. Park, B. Greig, and J. B. Muñoz, A tale of two sites—I. Inferring the properties of minihalo-hosted galaxies from current observations, *Mon. Not. R. Astron. Soc.* **495**, 123 (2020).
- [16] Y. Qin, A. Mesinger, B. Greig, and J. Park, A tale of two sites—II. Inferring the properties of minihalo-hosted galaxies with upcoming 21-cm interferometers, *Mon. Not. R. Astron. Soc.* **501**, 4748 (2021).
- [17] I. Reis, R. Barkana, and A. Fialkov, Mapping discrete galaxies at cosmic dawn with 21 cm observations, *Astrophys. J.* **933**, 51 (2022).
- [18] Q.-B. Ma, R. Ghara, B. Ciardi, I. T. Iliev, L. V. E. Koopmans, G. Mellema, R. Mondal, and S. Zaroubi, POLAR—I: linking the 21-cm signal from the epoch of reionization to galaxy formation, *Mon. Not. R. Astron. Soc.* **522**, 3284 (2023).
- [19] A. Lidz, O. Zahn, S. Furlanetto, M. McQuinn, L. Hernquist, and M. Zaldarriaga, Probing reionization with the 21 cm-galaxy cross power spectrum, *Astrophys. J.* **690**, 252 (2009).
- [20] R. P. C. Wiersma *et al.*, LOFAR insights into the epoch of reionization from the cross power spectrum of 21 cm emission and galaxies, *Mon. Not. R. Astron. Soc.* **432**, 2615 (2013).
- [21] H. Jensen *et al.*, Probing reionization with LOFAR using 21-cm redshift space distortions, *Mon. Not. R. Astron. Soc.* **435**, 460 (2013).
- [22] P. D. Meerburg, C. Dvorkin, and D. N. Spergel, Probing patchy reionization through $\tau - 21$ cm correlation statistics, *Astrophys. J.* **779**, 124 (2013).
- [23] B. Greig and A. Mesinger, 21 CMMC: An MCMC analysis tool enabling astrophysical parameter studies of the cosmic 21 cm signal, *Mon. Not. R. Astron. Soc.* **449**, 4246 (2015).
- [24] B. Greig and A. Mesinger, Simultaneously constraining the astrophysics of reionization and the epoch of heating with 21 CMMC, *Mon. Not. R. Astron. Soc.* **472**, 2651 (2017).
- [25] M. Kolopanis *et al.*, A simplified, lossless re-analysis of PAPER-64, *Astrophys. J.* **883**, 133 (2019).
- [26] B. Greig, C. M. Trott, N. Barry, S. J. Mutch, B. Pindor, R. L. Webster, and J. S. B. Wyithe, Exploring reionization and high- z galaxy observables with recent multiredshift MWA upper limits on the 21-cm signal, *Mon. Not. R. Astron. Soc.* **500**, 5322 (2020).
- [27] R. Ghara *et al.*, Constraining the intergalactic medium at $z \approx 9.1$ using LOFAR epoch of reionization observations, *Mon. Not. R. Astron. Soc.* **493**, 4728 (2020).
- [28] C. A. Watkinson, B. Greig, and A. Mesinger, Epoch of reionization parameter estimation with the 21-cm bispectrum, *Mon. Not. R. Astron. Soc.* **510**, 3838 (2022).
- [29] M. Rahimi *et al.*, Epoch of reionization power spectrum limits from Murchison Widefield array data targeted at EoR1 field, *Mon. Not. R. Astron. Soc.* **508**, 5954 (2021).
- [30] Y. Qin, A. Mesinger, S. E. I. Bosman, and M. Viel, Reionization and galaxy inference from the high-redshift Ly α forest, *Mon. Not. R. Astron. Soc.* **506**, 2390 (2021).
- [31] A. Saxena, A. Cole, S. Gazagnes, P. D. Meerburg, C. Weniger, and S. J. Witte, Constraining the x-ray heating and reionization using 21-cm power spectra with marginal neural ratio estimation, *Mon. Not. R. Astron. Soc.* **525**, 6097 (2023).
- [32] X.-L. Chen and J. Miralda-Escude, The spin-kinetic temperature coupling and the heating rate due to Lyman-alpha scattering before reionization: Predictions for 21 cm emission and absorption, *Astrophys. J.* **602**, 1 (2004).
- [33] A. Mesinger, A. Ewall-Wice, and J. Hewitt, Reionization and beyond: Detecting the peaks of the cosmological 21 cm signal, *Mon. Not. R. Astron. Soc.* **439**, 3262 (2014).
- [34] R. Ghara and G. Mellema, Impact of Ly α heating on the global 21-cm signal from the cosmic dawn, *Mon. Not. R. Astron. Soc.* **492**, 634 (2020).
- [35] B. Greig *et al.*, Interpreting LOFAR 21-cm signal upper limits at $z \approx 9.1$ in the context of high- z galaxy and reionization observations, *Mon. Not. R. Astron. Soc.* **501**, 1 (2021).
- [36] R. Ghara, S. K. Giri, B. Ciardi, G. Mellema, and S. Zaroubi, Constraining the state of the intergalactic medium during the epoch of reionization using MWA 21-cm signal observations, *Mon. Not. R. Astron. Soc.* **503**, 4551 (2021).
- [37] B. Maity and T. R. Choudhury, Probing the thermal history during reionization using a seminumerical photon-conserving code script, *Mon. Not. R. Astron. Soc.* **511**, 2239 (2022).
- [38] Z. Abdurashidova *et al.* (HERA Collaboration), HERA Phase I limits on the cosmic 21 cm signal: Constraints on astrophysics and cosmology during the epoch of reionization, *Astrophys. J.* **924**, 51 (2022).
- [39] Z. Abdurashidova *et al.* (HERA Collaboration), Improved constraints on the 21 cm EoR power spectrum and the x-ray heating of the IGM with HERA Phase I observations, *Astrophys. J.* **945**, 124 (2023).
- [40] H. Lazare, D. Sarkar, and E. D. Kovetz, HERA bound on x-ray luminosity weakens when accounting for population III stars, [arXiv:2307.15577](https://arxiv.org/abs/2307.15577).
- [41] R. A. Monsalve, A. Fialkov, J. D. Bowman, A. E. E. Rogers, T. J. Mozdzen, A. Cohen, R. Barkana, and N. Mahesh, Results from EDGES high-band: III. New constraints on parameters of the early Universe, *Astrophys. J.* **875**, 67 (2019).
- [42] J. Nambissan T., R. Subrahmanyam, R. Somashekar, N. Udaya Shankar, S. Singh, A. Raghunathan, B. S. Girish, K. S. Srivani, and M. Sathyanarayana Rao, SARAS 3 CD/EoR radiometer: Design and performance of the receiver, [arXiv:2104.01756](https://arxiv.org/abs/2104.01756).
- [43] E. de Lera Acedo *et al.*, The REACH radiometer for detecting the 21-cm hydrogen signal from redshift $z \approx 7.5-28$, *Nat. Astron.* **6**, 998 (2022).
- [44] D. C. Price *et al.*, Design and characterization of the large-aperture experiment to detect the dark age (LEDA) radiometer systems, *Mon. Not. R. Astron. Soc.* **478**, 4193 (2018).

- [45] L. Philip, Z. Abdurashidova, H. C. Chiang, N. Ghazi, A. Gumba, H. M. Heilgendorff, J. M. Jáuregui-García, K. Malepe, C. D. Nunhokee, J. Peterson, J. L. Sievers, V. Simes, and R. Spann, Probing radio intensity at high- Z from Marion: 2017 instrument, *J. Astron. Instrum.* **8**, 1950004 (2019).
- [46] F. G. Mertens *et al.*, Improved upper limits on the 21-cm signal power spectrum of neutral hydrogen at $z \approx 9.1$ from LOFAR, *Mon. Not. R. Astron. Soc.* **493**, 1662 (2020).
- [47] S. Yoshiura *et al.*, A new MWA limit on the 21 cm power spectrum at redshifts ~ 13 –17, *Mon. Not. R. Astron. Soc.* **505**, 4775 (2021).
- [48] S. Pal, S. Bharadwaj, A. Ghosh, and S. Choudhuri, Demonstrating the tapered gridded estimator (TGE) for the cosmological H I 21-cm power spectrum using 150-MHz GMRT observations, *Mon. Not. R. Astron. Soc.* **501**, 3378 (2021).
- [49] A. R. Parsons *et al.*, New limits on 21 cm EoR from PAPER-32 consistent with an x-ray heated IGM at $z = 7.7$, *Astrophys. J.* **788**, 106 (2014).
- [50] Z. Abdurashidova *et al.* (HERA Collaboration), First results from HERA phase I: Upper limits on the epoch of reionization 21 cm power spectrum, *Astrophys. J.* **925**, 221 (2022).
- [51] R. Braun, T. Bourke, J. A. Green, E. Keane, and J. Wagg, Advancing astrophysics with the square kilometre array, *Proc. Sci. AASKA14* (2015) 174.
- [52] S. Jester and H. Falcke, Science with a lunar low-frequency array: From the dark ages of the Universe to nearby exoplanets, *New Astron. Rev.* **53**, 1 (2009).
- [53] J. O. Burns, G. Hallinan, J. Lux, L. Teitelbaum, J. Kocz, R. MacDowall, R. Bradley, D. Rapetti, W. Wu, S. Furlanetto, A. Austin, A. Romero-Wolf, T.-C. Chang, J. Bowman, J. Kasper, M. Anderson, Z. Zhen, J. Pober, and J. Mirocha, NASA probe study report: Farside array for radio science investigations of the dark ages and exoplanets (FARSIDE), [arXiv:1911.08649](https://arxiv.org/abs/1911.08649).
- [54] S. Furlanetto *et al.*, Astro 2020 science white paper: Fundamental cosmology in the dark ages with 21-cm line fluctuations, [arXiv:1903.06212](https://arxiv.org/abs/1903.06212).
- [55] J. Silk, The limits of cosmology: Role of the Moon, *Phil. Trans. A. Math. Phys. Eng. Sci.* **379**, 20190561 (2021).
- [56] J. Burns *et al.*, Global 21-cm cosmology from the farside of the moon, [arXiv:2103.05085](https://arxiv.org/abs/2103.05085).
- [57] J. Burns *et al.*, A lunar farside low radio frequency array for dark ages 21-cm cosmology, [arXiv:2103.08623](https://arxiv.org/abs/2103.08623).
- [58] A. Goel *et al.*, Probing the cosmic dark ages with the lunar crater radio telescope, [arXiv:2205.05745](https://arxiv.org/abs/2205.05745).
- [59] Y. Shi, F. Deng, Y. Xu, F. Wu, Q. Yan, and X. Chen, Lunar orbit measurement of the cosmic dawn's 21 cm global spectrum, *Astrophys. J.* **929**, 32 (2022).
- [60] G. Bertone, O. L. Buchmueller, and P. S. Cole, Perspectives on fundamental cosmology from low Earth orbit and the moon, *npj Microgravity* **9**, 10 (2023).
- [61] A. Loeb and M. Zaldarriaga, Measuring the small-scale power spectrum of cosmic density fluctuations through 21 cm tomography prior to the epoch of structure formation, *Phys. Rev. Lett.* **92**, 211301 (2004).
- [62] J. Flitter and E. D. Kovetz, preceding paper, New tool for 21-cm cosmology. I. Probing Λ CDM and beyond, *Phys. Rev. D* **109**, 043512 (2024).
- [63] A. Mesinger, S. Furlanetto, and R. Cen, 21 cmFAST: A fast, semi-numerical simulation of the high-redshift 21-cm signal, *Mon. Not. R. Astron. Soc.* **411**, 955 (2011).
- [64] J. B. Muñoz, Y. Qin, A. Mesinger, S. G. Murray, B. Greig, and C. Mason, The impact of the first galaxies on cosmic dawn and reionization, *Mon. Not. R. Astron. Soc.* **511**, 3657 (2022).
- [65] D. Blas, J. Lesgourgues, and T. Tram, The cosmic linear anisotropy solving system (CLASS) II: Approximation schemes, *J. Cosmol. Astropart. Phys.* **07** (2011) 034.
- [66] J. B. Muñoz, An effective model for the cosmic-dawn 21-cm signal, *Mon. Not. R. Astron. Soc.* **523**, 2587 (2023).
- [67] A. Lewis and A. Challinor, The 21 cm angular-power spectrum from the dark ages, *Phys. Rev. D* **76**, 083005 (2007).
- [68] N. Aghanim *et al.* (Planck Collaboration), Planck 2018 results. VI. Cosmological parameters, *Astron. Astrophys.* **641**, A6 (2020); **652**, C4(E) (2021).
- [69] T. Venumadhav, L. Dai, A. Kaurov, and M. Zaldarriaga, Heating of the intergalactic medium by the cosmic microwave background during cosmic dawn, *Phys. Rev. D* **98**, 103513 (2018).
- [70] C. M. Hirata, Wouthuysen-field coupling strength and application to high-redshift 21 cm radiation, *Mon. Not. R. Astron. Soc.* **367**, 259 (2006).
- [71] I. Reis, A. Fialkov, and R. Barkana, The subtlety of Ly α photons: changing the expected range of the 21-cm signal, *Mon. Not. R. Astron. Soc.* **506**, 5479 (2021).
- [72] D. Sarkar, J. Flitter, and E. D. Kovetz, Exploring delaying and heating effects on the 21-cm signature of fuzzy dark matter, *Phys. Rev. D* **105**, 103529 (2022).
- [73] Y. Ali-Haïmoud and C. M. Hirata, HyRec: A fast and highly accurate primordial hydrogen and helium recombination code, *Phys. Rev. D* **83**, 043513 (2011).
- [74] N. Lee and Y. Ali-Haïmoud, HyRec-2: A highly accurate sub-millisecond recombination code, *Phys. Rev. D* **102**, 083517 (2020).
- [75] P. J. E. Peebles, Recombination of the primeval plasma, *Astrophys. J.* **153**, 1 (1968).
- [76] Y. Ali-Haïmoud, P. D. Meerburg, and S. Yuan, New light on 21 cm intensity fluctuations from the dark ages, *Phys. Rev. D* **89**, 083506 (2014).
- [77] S. Weinberg, Adiabatic modes in cosmology, *Phys. Rev. D* **67**, 123504 (2003).
- [78] D. Pequignot, P. Petitjean, and C. Boisson, Total and effective radiative recombination coefficients, *Astron. Astrophys.* **251**, 680 (1991).
- [79] S. Seager, D. D. Sasselov, and D. Scott, A new calculation of the recombination epoch, *Astrophys. J. Lett.* **523**, L1 (1999).
- [80] S. Seager, D. D. Sasselov, and D. Scott, How exactly did the Universe become neutral?, *Astrophys. J. Suppl. Ser.* **128**, 407 (2000).
- [81] J. A. Rubiño-Martín, J. Chluba, W. A. Fendt, and B. D. Wandelt, Estimating the impact of recombination uncertainties on the cosmological parameter constraints from cosmic microwave background experiments, *Mon. Not. R. Astron. Soc.* **403**, 439 (2010).

- [82] J. B. Muñoz, Y. Ali-Haïmoud, and M. Kamionkowski, Primordial non-Gaussianity from the bispectrum of 21-cm fluctuations in the dark ages, *Phys. Rev. D* **92**, 083508 (2015).
- [83] S. G. Murray, POWERBOX: A PYTHON package for creating structured fields with isotropic power spectra, *J. Open Source Software* **3**, 850 (2018).
- [84] S. Dodelson, *Modern Cosmology* (Academic Press, Amsterdam, 2003).
- [85] D. Baumann, *Cosmology* (Cambridge University Press, Cambridge, England, 2022), 10.1017/9781108937092.
- [86] Y. Mao, P. R. Shapiro, G. Mellema, I. T. Iliev, J. Koda, and K. Ahn, Redshift space distortion of the 21 cm background from the epoch of reionization I: Methodology re-examined, *Mon. Not. R. Astron. Soc.* **422**, 926 (2012).
- [87] P. Virtanen *et al.* (SciPy 1.0 Contributors), SciPy1.0: Fundamental algorithms for scientific computing in PYTHON, *Nat. Methods* **17**, 261 (2020).
- [88] J. L. Friedman and B. F. Schutz, Lagrangian perturbation theory of nonrelativistic fluids, *Astrophys. J.* **221**, 937 (1978).
- [89] T. Buchert, A class of solutions in Newtonian cosmology and the pancake theory, *Astron. Astrophys.* **223**, 9 (1989), <https://ui.adsabs.harvard.edu/abs/1989A%26A...223....9B/abstract>.
- [90] F. Moutarde, J. M. Alimi, F. R. Bouchet, R. Pellat, and A. Ramani, Precollapse scale invariance in gravitational instability, *Astrophys. J.* **382**, 377 (1991).
- [91] T. Buchert, Lagrangian perturbation theory—A key-model for large-scale structure, *Astron. Astrophys.* **267**, L51 (1993), <https://ui.adsabs.harvard.edu/abs/1993A%26A...267L..51B/abstract>.
- [92] E. Hivon, F. R. Bouchet, S. Colombi, and R. Juszkiewicz, Redshift distortions of clustering: A Lagrangian approach, *Astron. Astrophys.* **298**, 643 (1995), <https://ui.adsabs.harvard.edu/abs/1995A%26A...298..643H/abstract>.
- [93] J. Carlson, M. White, and N. Padmanabhan, A critical look at cosmological perturbation theory techniques, *Phys. Rev. D* **80**, 043531 (2009).
- [94] T. Tatekawa, Lagrangian perturbation theory in Newtonian cosmology, *Recent Res. Dev. Phys. Chem.* **2**, 1 (2005), <https://ui.adsabs.harvard.edu/abs/2004astro.ph.12025T/abstract>.
- [95] Y. B. Zel'dovich, Gravitational instability: An approximate theory for large density perturbations, *Astron. Astrophys.* **5**, 84 (1970), <https://ui.adsabs.harvard.edu/abs/1970A%26A....5...84Z/abstract>.
- [96] M. White, The Zel'dovich approximation, *Mon. Not. R. Astron. Soc.* **439**, 3630 (2014).
- [97] J. Hidding, S. F. Shandarin, and R. van de Weygaert, The Zel'dovich approximation: Key to understanding cosmic web complexity, *Mon. Not. R. Astron. Soc.* **437**, 3442 (2014).
- [98] G. Efstathiou, M. Davis, S. D. M. White, and C. S. Frenk, Numerical techniques for large cosmological N-body simulations, *Astrophys. J.* **57**, 241 (1985).
- [99] E. Sirko, Initial conditions to cosmological N-body simulations, or how to run an ensemble of simulations, *Astrophys. J.* **634**, 728 (2005).
- [100] A. Mesinger and S. Furlanetto, Efficient simulations of early structure formation and reionization, *Astrophys. J.* **669**, 663 (2007).
- [101] R. Scoccimarro, Transients from initial conditions: A perturbative analysis, *Mon. Not. R. Astron. Soc.* **299**, 1097 (1998).
- [102] S. Naoz and R. Barkana, Growth of linear perturbations before the era of the first galaxies, *Mon. Not. R. Astron. Soc.* **362**, 1047 (2005).
- [103] D. Tseliakhovich, R. Barkana, and C. Hirata, Suppression and spatial variation of early galaxies and minihalos, *Mon. Not. R. Astron. Soc.* **418**, 906 (2011).
- [104] D. Tseliakhovich and C. Hirata, Relative velocity of dark matter and baryonic fluids and the formation of the first structures, *Phys. Rev. D* **82**, 083520 (2010).
- [105] A. Fialkov, R. Barkana, D. Tseliakhovich, and C. M. Hirata, Impact of the relative motion between the dark matter and baryons on the first stars, *Mon. Not. R. Astron. Soc.* **424**, 1335 (2012).
- [106] B. Greig and A. Mesinger, 21 CMMC with a 3D light-cone: The impact of the co-evolution approximation on the astrophysics of reionization and cosmic dawn, *Mon. Not. R. Astron. Soc.* **477**, 3217 (2018).
- [107] M. McQuinn, O. Zahn, M. Zaldarriaga, L. Hernquist, and S. R. Furlanetto, Cosmological parameter estimation using 21 cm radiation from the epoch of reionization, *Astrophys. J.* **653**, 815 (2006).
- [108] R. Barkana and A. Loeb, Light-cone anisotropy in 21 cm fluctuations during the epoch of reionization, *Mon. Not. R. Astron. Soc.* **372**, L43 (2006).
- [109] K. Zawada, B. Semelin, P. Vonlanthen, S. Baek, and Y. Revaz, Light-cone anisotropy in the 21 cm signal from the epoch of reionization, *Mon. Not. R. Astron. Soc.* **439**, 1615 (2014).
- [110] K. K. Datta, G. Mellema, Y. Mao, I. T. Iliev, P. R. Shapiro, and K. Ahn, Light cone effect on the reionization 21-cm power spectrum, *Mon. Not. R. Astron. Soc.* **424**, 1877 (2012).
- [111] K. K. Datta, H. Jensen, S. Majumdar, G. Mellema, I. T. Iliev, Y. Mao, P. R. Shapiro, and K. Ahn, Light cone effect on the reionization 21-cm signal II: Evolution, anisotropies and observational implications, *Mon. Not. R. Astron. Soc.* **442**, 1491 (2014).
- [112] P. La Plante, N. Battaglia, A. Natarajan, J. B. Peterson, H. Trac, R. Cen, and A. Loeb, Reionization on large scales IV: Predictions for the 21 cm signal incorporating the light cone effect, *Astrophys. J.* **789**, 31 (2014).
- [113] R. Ghara, K. K. Datta, and T. R. Choudhury, 21 cm signal from cosmic dawn—II. Imprints of the light-cone effects, *Mon. Not. R. Astron. Soc.* **453**, 3143 (2015).
- [114] R. Mondal, S. Bharadwaj, and K. K. Datta, Towards simulating and quantifying the light-cone EoR 21-cm signal, *Mon. Not. R. Astron. Soc.* **474**, 1390 (2018).
- [115] <https://github.com/21cmfast/21cmFAST>.
- [116] https://github.com/lesgourg/class_public.
- [117] <https://github.com/cmbant/CAMB>.
- [118] <https://github.com/nanoomlee/HYREC-2>.
- [119] <https://github.com/steven-murray/powerbox>.
- [120] L. Senatore, S. Tassev, and M. Zaldarriaga, Cosmological perturbations at second order and recombination perturbed, *J. Cosmol. Astropart. Phys.* **08** (2009) 031.

-
- [121] B. Zygelman, Hyperfine level-changing collisions of hydrogen atoms and tomography of the dark age universe, *Astrophys. J.* **622**, 1356 (2005).
- [122] S. Furlanetto and M. Furlanetto, Spin exchange rates in electron-hydrogen collisions, *Mon. Not. R. Astron. Soc.* **374**, 547 (2007).
- [123] S. Furlanetto and M. Furlanetto, Spin exchange rates in proton-hydrogen collisions, *Mon. Not. R. Astron. Soc.* **379**, 130 (2007).
- [124] A. Fialkov and R. Barkana, Signature of excess radio background in the 21-cm global signal and power spectrum, *Mon. Not. R. Astron. Soc.* **486**, 1763 (2019).